Nano-engineering of High Harmonic Generation in Solid State Systems

By
Shaimaa Almalki

A thesis submitted to the Faculty of Graduate and Postdoctoral Studies in partial fulfilment of the requirements for the degree of Doctorate of Philosophy in Physics

Department of Physics
Faculty of Science
University of Ottawa

List of Publications

1. S Almalki, AM Parks, G Bart, PB Corkum, T Brabec, and CR McDonald. High harmonic generation tomography of impurities in solids: Conceptual analysis. Physical Review B, 98(14):144307, 2018.
2. S Almalki, AM Parks, T Brabec, and CR McDonald. Nanoengineering of strong field processes in solids. Journal of Physics B: Atomic, Molecular and Optical Physics, 51(8):084001, 2018.
3. CR McDonald, KS Amin, S Almalki, and T Brabec. Enhancing high harmonic output in solids through quantum confinement. Physical review letters, 119(18):183902, 2017.

Contents

List of Figures

Abstract

High harmonic generation (HHG) in solids has two main applications. First, HHG is an all-solid-state source of coherent attosecond very ultraviolet (VUV) radiation. As such, it presents a promising source for attosecond science. The ultimate goal of attosecond science is to make spatially and temporally resolved movies of microscopic processes, such as the making and breaking of molecular bonds. Second, the HHG process itself can be used to spatially and temporally resolve fast processes in the condensed matter phase, such as charge shielding, multi-electron interactions, and the dynamics and decay of collective excitations. The main obstacles to realize these goals are: the very low efficiency of HHG in solids and incomplete understanding of the ultrafast dynamics of the complex many-body processes occurring in the condensed matter phase.

The theoretical analysis developed in this thesis promises progress along both directions. First, it is demonstrated that nanoengineering by using lower-dimensional solids can drastically enhance the efficiency of HHG. The effect of quantum confinement on HHG in semiconductor materials is studied by systematically varying the confinement width along one and two directions transverse to the laser polarization. Our analysis shows growth in high harmonic efficiency concurrent with a reduction of ionization. This decrease in ionization comes as a consequence of an increased band gap resulting from the confinement. The increase in harmonic efficiency results from a restriction of wave packet spreading, leading to greater re-collision probability. Consequently, nanoengineering of one and two-dimensional nanosystems may prove to be a viable means to increase harmonic yield and photon energy in semiconductor materials driven by intense laser fields. Thus, it will contribute towards the development of reliable, all-solid-state, small-scale, and laboratory attosecond pulse sources.

Second, it is shown that HHG from impurities can be used to tomographically reconstruct impurity orbitals. A quasi-classical three-step model is developed that builds a basis for impurity tomography. HHG from impurities is found to be similar to the high harmonic generation in atomic and molecular gases with the main difference coming from the non-parabolic nature of the bands. This opens a new

avenue for strong field atomic and molecular physics in the condensed matter phase and allows many of the processes developed for gas-phase attosecond science to be applied to the condensed matter phase. As a first application, my conceptual study demonstrates the feasibility of tomographic measurement of impurity orbitals. Ultimately, this could result in temporally and spatially resolved measurements of electronic processes in impurities with potential relevance to quantum information sciences, where impurities are prime candidates for realizing qubits and single photon sources. Although scanning tunneling microscope (STMs) can measure electron charge distributions in impurities, measurements are limited to the first few surface layers and ultrafast time resolution is not possible yet. As a result, HHG tomography can add complementary capacities to the study of impurities.

Acknowledgements

All praise the Almighty Allah for giving me the strength and ability to complete this journey.

There are no words that can express my deep gratitude to my brother, Abdull-Rahman, not only for accompanying me but also for all his sacrifices, encouragement, and patience. Most of all my appreciation goes to my parents and siblings for their unconditional love, endless support, and prayers.

I wish to thank my supervisor, Prof. Thomas Brabec, for giving me the opportunity to be in his research group and for continuous support. I would also like to express my thanks to Dr. Chris McDonald for his advice, assistance in keeping my progress on schedule and helping in numerical analysis. Special thanks to Azza bin Taher, the ex-member of our group, for all nights we spent studying together in the office.

I would like to thank each of the faculty members who give me the chance to be a teaching assistant for them: Dr. Michael Wong, Dr. Andrzej Czajkowski, and Dr. Peter Piercy.

My sincere thanks are also extended to the Ministry of Education in Saudi Arabia represented by the Saudi Arabian Cultural Bureau in Canada for financial support. I owe thanks to my advisors in the bureau, Mrs. Nancy Jad and Dr. Ziyad Jasim for their insightful advice and constant kindness.

Finally, my grateful thank goes to my friend, Aisha Okmi, for understanding, supporting, and being a good listener whenever I need to babble. Thanks also to my friend, Norah Alotubi, and her beloved daughter, Dalal, for all great time I have spent with them in Ottawa.

Introduction

Nearly a quarter century has passed since the re-collision picture for atomic systems exposed to intense-laser fields came into focus [1]. In particular, this picture provided a simple mechanism through which the process of high harmonic generation (HHG) could be viewed — the three-step model. Here an electron is (i) brought up into the continuum, (ii) accelerated away from its parent ion by the electric field of the laser and then driven back when the field changes direction, resulting in (iii) re-collision with the parent ion. This re-collision results in the emission of coherent radiation that has a frequency that is many multiples of the driving frequency of the laser. Ultimately, this understanding led to the emergence of attosecond science [2]. As recollision takes place during a fraction of the laser half-cycle, attosecond pulses are generated. The Holy Grail of attosecond science is to make movies of fundamental microscopic processes, such as the making and breaking of chemical bonds. HHG takes a central role in attosecond science, as a source for attosecond pulses and also as a direct measurement method for ultrafast processes. Additional processes occur during recollision and rescattering [3], such as nonsequential double ionization, above-threshold ionization, and laser-induced electron diffraction [4–7]; these processes also contain structural information and are additional examples of how the three-step process of HHG can be used to directly probe ultrafast dynamics in the matter.

Recent experiments with mid-infrared [8–11] and THz pump sources [12–14] have demonstrated HHG in solids. The theoretical study has identified two mechanisms [15, 16]; (i) intraband HHG due to the non-parabolic nature of bands [9] was found to be dominant in dielectrics; (ii) interband HHG dominates in semiconductors and is created in a three-step process similar to atomic and molecular HHG [17]. This similarity provides an avenue through which the above-discussed tools and techniques of attosecond science developed for atomic and molecular systems can be applied to solid state physics.

There are two main motivations to study HHG in the condensed matter phase. First, an all-solid-state attosecond radiation source is very attractive. Second, sim-

ilar to atomic and molecular gases, there are ultrafast and ultrafine processes in solids that can be resolved with HHG directly or with attosecond pulses. The main obstacles to achieving these goals are a too low HHG efficiency in solids and a far from complete theoretical understanding of the dynamic interaction of intense laser fields with solids. One of the advantages to working with solids over atomic gases is that the properties of solids can be changed by doping, reducing dimensionality and altering the morphology of the material. Recently, HHG in two-dimensional solids has been experimentally demonstrated [18]. In addition, HHG involving solid state systems with impurities has been considered [19, 20]. The goal of this dissertation is to extend our theory knowledge from HHG in solids to HHG in nano-engineered systems, such as low-dimensional solids and impurity doped materials. In the first part of the thesis, strong field physics and HHG in low dimensional systems such as quantum wires and quantum sheets will be investigated. In the second part, the theory of HHG in bulk semiconductors with shallow donor states is developed and applied to study the tomographic reconstruction of impurity orbitals from harmonic spectra. Thus, my thesis contributes to the two main motivations outlined above, as will be explained in more detail in the remainder of this section.

For HHG, in both atoms and solids, to be viable for attosecond applications, the amount of harmonic output and the maximum photon energy that can be produced must be considered. To understand the limitations, HHG has to be considered from a microscopic (single atom in laser) and a macroscopic (wave propagation in atomic gas) viewpoint. Both parts underlie different limitations. The microscopic efficiency is determined by the amount of ionization per laser half cycle and the part of the free electron wavepacket that recombines with the parent ion during recollision. Recombination is strongly influenced by quantum diffusion, i.e. the electron wavepacket born by tunnel ionization spreads during its excursion in the continuum. Once it recollides with the parent ion, only a tiny fraction of the wavepacket overlaps with the parent ion ground state, resulting in low quantum efficiencies. Quantum diffusion grows in strength with increasing excursion amplitude which increases with higher pump laser intensity and longer wavelength. Quantum diffusion presents a fundamental limitation in both gases and solids.

The macroscopic component of HHG is limited by phase mismatch between pump laser and harmonic beam and by reabsorption of harmonic radiation. Reabsorption in gases does not play a dominant role due to their comparatively low atom density (up to 10^{19} atoms/cm^3). HHG in gases is dominantly limited by phase mismatch due to the different refractive indices experienced by the pump laser and harmonic signal. By contrast, reabsorption is the dominant limiting mechanism in solids due to the significantly higher densities, and phase mismatch does not play any role.

What has so far been done to increase harmonic pulse and photon energies?

One method of obtaining higher photon energies is to increase the peak field intensity and/or wavelength of the driving laser. Whether the harmonic pulse energy increases with increasing laser intensity is a more subtle question and has to be treated on a case by case basis. There is a limit to how much the pump laser intensity and therewith harmonic photon energy can be increased. In gases, it is set by the depletion of ionization, whereas in solids is determined by the onset of material damage. Increase in pump wavelength results in longer excursion amplitudes and stronger quantum diffusion resulting in a reduction of harmonic efficiency. It has been demonstrated that by confining the system transversely with a magnetic field HHG in gases can be increased [21]. However, so far the effects of quantum diffusion have turned out to be very difficult to compensate for. Quantum diffusion also limits interband HHG in solids [15, 16]. HHG in semiconductors requires low wavelength pulse lasers in the mid-infrared wavelength regime. The resulting large electron excursion amplitude results in strong quantum spreading of the electron wavepacket and small recollision probabilities.

Various phase matching methods have been developed for HHG in gases. They work well for individual narrow band harmonics, however are difficult to realize over the wide spectrum of attosecond pulses. In solids, harmonic propagation is dominated by absorption losses from deeper bound core-level electrons; phase mismatch effects can be neglected. So far, no remedy has been found for absorption losses. In the condensed matter phase, quantum diffusion and absorption losses are the two main limiting effects of HHG.

One of the main findings of my thesis is that recollision and thus HHG can be increased in low dimensional quantum systems. The effect of quantum confinement along one or two transverse directions will restrict the motion of carriers along these directions. This, in turn, restricts quantum diffusion and reduces wave packet spreading during the quiver motion of the electron-hole pair, leading to a more significant recollision cross-section. Potentially, stacked lower dimensional systems, such as a quantum wire forest, might also contribute to lifting the second limitation. In such systems, harmonics are generated in the low-dimensional material, however propagation occurs also in the gaps between the material layers, where no reabsorption exists. This point will be subject to further research. The first part of my thesis contributes to enhancing high harmonic efficiency in solids bringing us closer to efficient all-solid-state table top attosecond sources.

As the physical pictures of HHG in gases and semiconductors are very similar, the hope is that attosecond technology can be transferred from gases to the solid state phase. One such example is the second major result of my thesis. It contributes to the second motivation point discussed above. The potential of applying molecular HHG tomography [22–24] to impurities is studied here. High harmonic

emission is considered directly from the impurity under a THz driving field. Because of the similarity between HHG in atoms and impurities, gas phase techniques can be translated into the condensed matter phase. Our result shows that HHG can be directly used as a spectroscopic method to resolve ultrafast processes involving impurities. As an example, tomographic reconstruction of the impurity ground state is demonstrated in a 1D model system. The impurity dipole moment is found to be the dominant factor in determining the magnitude of the harmonic signal as a function of harmonic order; ionization and propagation which have to be factored out in molecular tomography play a lesser role here. This indicates substantial facilitation due to the potential for direct reconstruction of the impurity ground state from the harmonic spectrum. High harmonic generation has been the bedrock on which attosecond spectroscopy techniques in gases have been built. These techniques have allowed for the study of the temporal and structural characteristics of atomic and molecular systems [25–28]. My thesis continues this work from the gas to the condensed matter phase.

The thesis is structured as follows. Chapter 1 is part of the introduction; the theory of high harmonic generation in atoms is introduced in more detail. In chapter 2, the theory of HHG in bulk solids is presented. The novel results are presented in chapters 3 and 4. The theoretical analysis of HHG in model nanostructures is introduced in chapter 3. The study of HHG from impurity ground state and the reconstruction of its wave function are shown in chapter 4.

All work presented here has been already published in the papers mentioned above in the list of publications. The theory of using nanowire to enhance the harmonic output was developed by T. Brabec and CR. McDonald. I worked on simulations and analysis of results and worked on the paper. I also made the main contributions to generalizing the results to thin layers in paper 2. In paper 3, I was the main researcher and was supported by T. Brabec and CR. McDonald to achieve the presented results.

Chapter 1

Harmonic generation in gas phase

In 1987, McPherson et al. [29] were the first to observe the harmonic spectrum generated from rare gases by intense ultraviolet (248 nm) radiation ($10^{15} - 10^{16}$ W/cm^2). The expectation at that time was to obtain an exponentially decreasing spectrum with harmonic orders. However, their unexpected result showed a harmonic spectrum that exponentially decreases at low order harmonics followed by a plateau that expands over several harmonic orders with approximately constant harmonic intensity. Then, there was a drop off region where the harmonic spectral intensity dramatically falls off. The interpretation of this behavior was given classically by Corkum et al. [1] and quantum mechanically by Lewenstein et al. [30] a few years later.

The goal of this chapter is to give a brief description of high harmonic generation and highlight the physics behind the three regions of its spectrum which are low-order harmonics, plateau, and cutoff.

1.1 Low-harmonic generation

When a conventional crystal medium is exposed to sufficiently high laser intensities, harmonics of the fundamental laser field can be generated. The phenomenon was first demonstrated by Franke *et al.* in 1961 [31]. The demonstration synchronized with the development of the laser, which created the required high-intensity coherent light. The production of harmonics is attributed to the laser-induced polarization of the medium $\mathbf{P}$(t) which has nonlinear dependence on the laser field $\mathbf{F}$(t). The response of the medium is given by

$$\mathbf{P}(t) = \epsilon_0\big(\chi^{(1)}\mathbf{F}(t) + \sum_{j>1}\chi^{(j)}\mathbf{F}^j(t)\big), \tag{1.1}$$

where χ is the electric susceptibility and ϵ_0 is the permittivity of free space. The first term in Equation (1.1) represents the linear polarization response. Other nonlinear terms become significant when the laser field strength roughly ranges between 10^8 to 10^{13} W/cm^2 [32]. Note that even-nonlinear processes cannot appear in a centrosymmetric material due to the inversion symmetry of the polarization and laser electric field. For such systems, only odd terms show up [33].

For simplicity's sake, the particle nature of the electron is usually used to describe the generation process. An electron jumps to higher real or virtual energy level by stimulated absorption. If the electron absorbs q photons from the laser field of frequency ω_0, it emits a single photon with $q\omega_0$ energy as it decays to its initial energy level. The output field intensity relies on the probability of having q-photon transitions, and it is proportional to the square of the atomic number density. Therefore, a high-intensity field can be achieved when the response of each atom constructively interferes which implies that the momentum is conserved. In other words, the phase-matching condition must be fulfilled, see Section 1.3.

1.1.1 Time-dependent perturbation theory

This approach is mainly based on treating the effects of the laser field on a quantum system as a perturbation. The following derivation is given in Refs. [34] and [33]. Here and throughout the rest of the thesis, the atomic units are used unless otherwise indicated, see Appendix D.

The Hamiltonian of the system in length gauge is assumed to be

$$H = H_0 + \lambda H', \tag{1.2}$$

where $H_0 = -\frac{1}{2}\nabla^2 + V(\mathbf{r})$ is the Hamiltonian of the atom before the presence of the laser field, λ is a small parameter, and $H' = -\mathbf{x}\cdot\mathbf{F}(t) = -\mathrm{x}F_0 e^{i\omega_0 t}$ is the interaction Hamiltonian. Let $|\psi_n^{(0)}(t)\rangle = e^{-i\omega_n t}|\phi_n^{(0)}\rangle$ be the eigenstates of H_0 with eigenvalues $E_n = \omega_n$. The perturbed states can be expanded as in terms of $|\psi_n^{(0)}(t)\rangle$ with probability amplitudes $a_l(t)$ as

$$|\psi_n(t)\rangle = \sum_l a_l(t)|\psi_n^{(0)}(t)\rangle = \sum_l a_l(t)e^{-i\omega_n t}|\phi_n^{(0)}\rangle, \tag{1.3}$$

where the probability amplitudes can be expressed as a sum of different order correction as

$$a_l(t) = \sum_m \lambda^m a_l^{(m)}(t) \tag{1.4}$$

Substituting Eq.(1.3) into time-dependent Schrödinger equation and multipling both sides by $e^{i\omega_k t}\langle\phi_k^{(0)}|$ gives the rate of probability amplitudes

$$i\partial_t a_k^{(m)}(t) = -F_0 \sum_l a_l^{(m-1)} \mathbf{x}_{kl} e^{i\omega_{kl}t}, \tag{1.5}$$

where $\mathbf{x}_{kl} = \langle\phi_k^{(0)}|\mathbf{x}|\phi_n^{(0)}\rangle$ is the dipole transition matrix and $\omega_{kl} = \omega_k - \omega_l - \omega_0$. To find $a_k^{(m)}$, one needs to find the the amplitude $a_l^{(m-1)}$ which is also defined by $a_p^{(m-2)}$. However, if $a_p^{(m-2)}$ is small compared to $a_l^{(m-1)}$, then the integration of $a_l^{(m-1)}$ can be approximated to

$$a_l^{(m-1)} = F_0 \sum_p \frac{a_p^{(m-2)} \mathbf{x}_{lp} e^{i\omega_{lp}}}{\omega_{lp}}. \tag{1.6}$$

Using Eq.(1.6) to rewrite Eq.(1.5) leads to

$$i\partial_t a_k^{(m)}(t) = -(F_0)^2 \sum_{l,p} \frac{a_p^{(m-2)} \mathbf{x}_{kl}\mathbf{x}_{lp}}{\omega_{lp}} e^{i(\omega_k - \omega_p - 2\omega_0)t}. \tag{1.7}$$

One still needs to find $a_p^{(m-2)}$, etc. Let us assume the transition from state l to state k is non-resonant and it occurs via intermidate states, $l_1, l_2, ..., l_{m-2}, l_{m-1}$. Each transition between these intermidiate states is a single-photon transition therefore the m^{th}-order of a_k can be written as

$$i\partial_t a_k^{(m)}(t) = -(F_0)^m \sum_{l_{m-1}, l_{m-2}, \ldots}^{l} \frac{\mathbf{x}_{kl_{m-1}}\mathbf{x}_{l_{m-1}l_{m-2}} \cdots \mathbf{x}_{l_1 l}}{\omega_{kl_{m-1}}\omega_{l_{m-1}l_{m-2}} \cdots \omega_{l_2 l_1}} e^{i(\omega_k - \omega_l - m\omega_0)t}. \tag{1.8}$$

Equation (1.8) represents a perturbative m-photon transition rate. The transition rate of population is then proportional to (I^m):

$$\Gamma^{(m)} \propto I^m. \tag{1.9}$$

Therefore, the probability of this process diminishes with the number of photons needed to excite the electron.

1.1.2 The breakdown of perturbation theory

The linear and lowest nonlinear orders of the probability amplitude can be deduced from Eq. (1.8). The evaluation of the integral gives

$$a_k^{(1)}(t) = F_0 \frac{\mathbf{x}_{kl}}{\omega_{kl}} e^{i\omega_{kl}t} \quad \text{, and} \tag{1.10}$$

$$a_k^{(2)}(t) = F_0^2 \sum_p \frac{\mathbf{x}_{kp} \cdot \mathbf{x}_{pl}}{\omega_{kp}(\omega_k - \omega_l - 2\omega_0)} e^{i(\omega_k - \omega_l - 2\omega_0)t}. \tag{1.11}$$

The linear polarization is given by

$$P^{(1)}(\omega_0) = N\left[\left\langle\psi_k^{(1)}|\mathbf{x}|\psi_l^{(0)}\right\rangle + \left\langle\psi_l^{(0)}|\mathbf{x}|\psi_k^{(1)}\right\rangle\right] \tag{1.12}$$

$$= NF_0\frac{\mathbf{x}_{kl}}{\omega_{lk}}\left[\mathbf{x}_{lk}e^{-i\omega_0 t} + \mathbf{x}_{kl}e^{i\omega_0 t}\right], \tag{1.13}$$

where N is the number density of atoms. From the relation $P(\omega_0) = \epsilon_0\chi(\omega_0)F(\omega_0)$, the linear susceptibility follows as

$$\chi^{(1)}(\omega_0) = \frac{N}{\epsilon_0}\frac{\mathbf{x}_{kl}}{\omega_{lk}}\left[\mathbf{x}_{lk} + \mathbf{x}_{kl}\right]. \tag{1.14}$$

If we assume that all electrons are initially in the ground state of the system, then $\chi^{(1)}(\omega_0)$ of a transition from state l to state k at low frequancy $\omega_l - \omega_k \gg \omega_0$ can be estimated to

$$\chi^{(1)} \simeq \frac{N}{\epsilon_0}\frac{|\mathrm{x}_{kl}|^2}{(\omega_l - \omega_k)}. \tag{1.15}$$

Following the same steps, the second order susceptibility can be approximated to [35]

$$\chi^{(2)} \simeq \frac{N}{\epsilon_0}\frac{\mathrm{x}_{lp}\mathrm{x}_{pk}\mathrm{x}_{kl}}{(\omega_p - \omega_l)(\omega_k - \omega_l)}. \tag{1.16}$$

If x_{mn} is equivalent to a typical value of electronic transitions ($\sim 10^{-29}$C.m) for any m and n states in the ultraviolt region ($\omega_{mn} = \omega_m - \omega_n \sim 0.5$ eV), then, the approximate ratio of the first order nonlinear polarization to the linear polarization yields

$$\left|\frac{P^{(2)}(\omega)}{P^{(1)}(\omega)}\right| = \left|\frac{\chi^{(2)}(\omega)F^2(\omega)}{\chi^{(1)}(\omega)F(\omega)}\right| \sim \frac{F_0\mathrm{x}_{mn}}{\omega_{mn}} \sim 10^{-9}F_0. \tag{1.17}$$

An incident electric field with an amplitude that is of the order of inner atomic fields ($\sim 10^9$V/cm) results in divergent series. This result can be generalized to include the ratio of any consecutive nonlinear terms. Therefore, the perturbative theory is unable to illustrate processes caused by a strong laser field. This failure was the reason behind seeking other approaches to describe the non-perturbative processes.

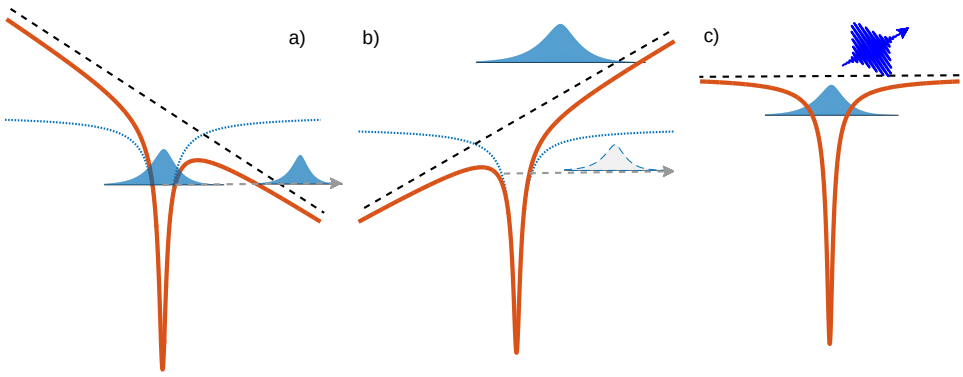

Figure 1.1: The three-step model: (a) tunnel ionization. (b) acceleration. (c) recombination.

1.2 High-harmonic generation

1.2.1 Semiclassical approach

The essence of high harmonic generation in gaseous media [36] can be semiclassically described by the so-called *three-step model* [1]. As shown in Fig. 1.1, the static potential of an atom is suppressed by the field strength of a short laser pulse in a way that allows the bound electron to penetrate through the potential barrier. Once the electron is free with zero initial velocity, it is accelerated away from the parent ion by the oscillating laser field and then driven back to it when the laser field reverses its direction. During this excursion, the electron moves in a classical trajectory and gains average energy called the *pondermotive energy* U_p which is the cycle-averaged kinetic energy of electrons freely oscillating in an electromagnetic field. In strong field approximation, the effect of the ionic potential is ignored throughout the propagation. When the electron recollides with the ion, it recombines and emits a harmonic photon. This process happens every half laser cycle; thus, harmonic energy photons are emitted twice per optical cycle which explains the fact of having odd spectral harmonics if the medium has inversion symmetry [33]. The following subsections are a more specific description of the three steps.

Tunnel ionization

When a low-frequency laser pulse irradiates an atom, several scenarios of ionization may happen based on the intensity of incident laser pulse. One process is multi-photon ionization (MPI) where more than one low-frequency photon is absorbed to

surmount the energy gap of ionization potential I_p. In the absence of resonances, the probability of this process diminishes with the number of photons needed to free the electron, see Eq.(1.9).

Tunnel ionization takes place when the electric field of the laser becomes comparable to interatomic field strength. In such cases, the potential of the laser field, $-\mathbf{F}(\mathrm{t})\cdot\mathbf{r}$, lowers the atomic Coulomb potential. The combination of the two potentials creates a finite barrier through which the electron can penetrate. As a tool for distinguishing between MPI and tunnel ionization, Keldysh [37] introduced a dimensionless parameter γ which can be written as

$$\gamma = \sqrt{\frac{I_p}{2U_p}}, \tag{1.18}$$

where $U_p = (F/2\omega_0)^2$ for a laser with frequency ω_0. Alternatively, the Keldysh parameter can be expressed as the ratio of tunneling time τ_k and the laser cycle, i.e., $\gamma = \tau_k\omega_0$. The tunneling time can be defined as the time that is required for the electron to pass through the barrier. Tunneling ionization occurs when the laser cycle is long compared to the tunneling time, $\gamma \ll 1$. That is, the electron sees a static barrier during its traversal. In the other extreme, $\gamma \gg 1$ multiphoton ionization is the dominant process.

Keldysh deduced the ionization rate of a hydrogen atom in an intense laser field in the quasi-static limit [37]. His analytical expression was extended to include arbitrary complex atoms later by Ammosov, Delone and Krainov (ADK) by using quasi-classical WKB (Wentzel-Kramers-Brilluoin) theory [38]. In the tunneling regime, their calculated ionization rate is given by

$$\mathrm{w}_{ADK} = \sqrt{\frac{3F_0}{\pi(2I_p)^{3/2}}}|C_{n^*l^*}|^2 G_{lm} I_p \left(\frac{2(2I_p)^{3/2}}{F_0}\right)^{n^*-|m|-1} \exp\left\{\left(-\frac{2(2I_p)^{3/2}}{3F_0}\right)\right\}, \tag{1.19}$$

where F_0 is the amplitude of the laser field, l is the angular momentum, and m is the magnetic quantum number. Further, $n^* = Z/\sqrt{2I_p}$ and $l^* = n^* - 1$ represent the effective principal and angular momentum quantum number, respectively, with Z being the ion charge. Moreover, the two coefficients $C_{n^*l^*}$ and G_{lm} are atomic parameters that depend on l and m. They are determined by matching the WKB solution of the under barrier wavefunction to the unperturbed atomic ground state.

Propagation

When the electron appears in the continuum at time t', the effect of the Coulomb potential can be considered negligible. This is a very reasonable approximation

regarding the strong laser electric field. Assuming a monochromatic and linearly polarized laser $\mathbf{F}(t) = F_0 \cos(\omega_0 t)\hat{\mathbf{x}}$, the velocity of an electron that tunnels and is born with zero initial velocity is

$$\mathrm{v}(t, t') = -F_0 \int_{t'}^{t} \cos(\omega_0 \tau) d\tau = -\frac{F_0}{\omega_0}[\sin(\omega_0 t) - \sin(\omega_0 t')]. \tag{1.20}$$

The electron momentum is equivalent to its velocity and can be rewritten as

$$\mathbf{k}(t, t') = \mathbf{A}(t) - \mathbf{A}(t'), \tag{1.21}$$

where $\mathbf{A}(t)$ is the vector potential of the laser field, $\mathbf{F}(t) = -\partial\mathbf{A}/\partial t$. Clearly, the average kinetic energy of the electron is proportional to laser intensity.

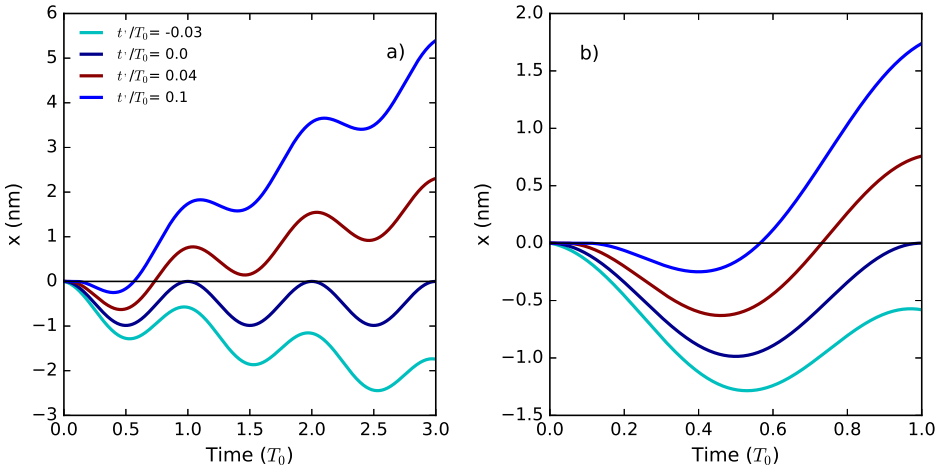

Figure 1.2: (a) Electron trajectories in a linearly polarized laser field born at different times. (b) A widened view of (a).

The position of the electron then is

$$x(t, t') = \frac{F_0}{\omega_0^2}[\cos(\omega_0 t) - \cos(\omega_0 t') + \sin(\omega_0 t')(t - t')]. \tag{1.22}$$

Figure 1.2 shows a plot of the electron position at different birth times t'. It shows that only some electron trajectories return to their parent ion. The trajectories intersections with the zero line represent the recombination. Therefore, the number of intersections represents the number of recombinations. An electron ionized at $t' = 0$ returns to its parent ion each laser cycle. For $t' \neq 0$, the later the time of birth, the sooner the electron returns. It is notable that all trajectories except the

one born at $t' = 0$ are pulled away during oscillation. That is due to the finite drift energy acquired by the electron during birth, see the second term in Eq. (1.20). Therefore, there is no recombination for electrons born before the peak of the laser field as long as the effect of Coulomb potential is ignored.

Recombination

When the electron recombines with its parent ion, it releases the energy gained during the propagation step by emitting a photon. Since the electron recombines with different velocities based on the time of birth, it gains different kinetic energies. The kinetic energy of the returning electron is determined by

$$T = 2U_p[\sin(\omega_0 t) - \sin(\omega_0 t')]^2. \tag{1.23}$$

Figure 1.3 shows the calculation of the kinetic energy as a function of the birth time. The maximal return energy is about $3.17U_p$, which is carried by the electron ionized at $0.05T_0$ and returns at $0.75T_0$. Therefore, the maximum emitted photon energy is

$$\omega_{max} = I_p + 3.17U_p. \tag{1.24}$$

where I_p is the ionization potential as was introduced earlier. Equation (1.24) represents the result of the analytical calculation of the *cutoff* law. It agrees with the experimental formula of the law introduced by Krause et al. [39].

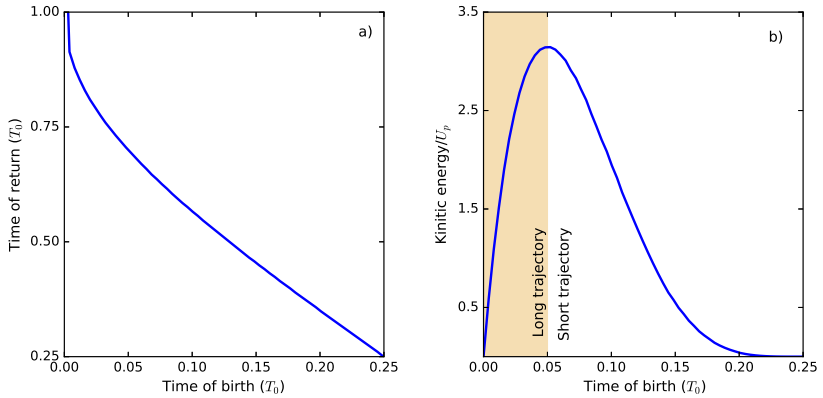

Figure 1.3: (a) Time of birth versus time of return. (b) The kinetic energy of the electron at the time of return as a function of the birth time. The shaded region indicate the kinetic energy of long electron trajectories

The cut-off energy separates two sets of trajectories that contribute to the same kinetic energy. Some electron trajectories are born after the birth of the electron that corresponds to the cut-off energy. Those trajectories are called the *short* trajectory because their excursion time is shorter than the excursion time of the cut-off energy τ_c. If the excursion time is longer than τ_c , then the trajectories are referred to as *long*.

1.2.2 Quantum approach

The quantum mechanical description of HHG was introduced by Lewenstein et al. [30]. It attributes the harmonic photon emission to the oscillating dipole of the medium. To find the dipole moment, one should start by solving the time-dependent Schrödinger equation in the single-active electron approximation (SEA) [40] where the effect of electron correlations is negligible. The Schrödinger equation is given by

$$i\partial_t \Psi(\mathbf{x},t) = (H_0 - \mathbf{x}.\mathbf{F}(t))\Psi(\mathbf{x},t), \tag{1.25}$$

where $H_0 = -\frac{1}{2}\nabla^2 + V(\mathbf{r})$ is the free field Hamiltonian. Lewenstein et al. solve Eq. (1.21) by using the Ansatz

$$|\Psi(t)\rangle = e^{iI_p t}(a(t)|0\rangle + \int d^3\mathbf{k} b(\mathbf{k},t)|\mathbf{k}\rangle), \tag{1.26}$$

where $\mathbf{k}$ is the electron momentum, $a(t)$ and $b(\mathbf{k},t)$ are the ground state and the continuum probability amplitudes, respectively. Adopting this wavefunction implies two things: (i) the potential of ions is ignored as soon as the electron is ionized, and (ii) there is no resonance with excited bound states. By inserting the Ansatz into the time-dependent Schrödinger equation and solving for the probability amplitude $b(\mathbf{k},t)$, the time-dependent dipole moment of the electron, $\mathbf{x}(t) = \langle \Psi(t)|\mathbf{x}|\Psi(t)\rangle$, is obtained as

$$\mathbf{x}(t) = \int_0^t dt' \int d^3\mathbf{k} \mathbf{F}(t') \cdot \mathbf{d}(\boldsymbol{\kappa}_t - \mathbf{A}(t')) e^{iS(\mathbf{k},t',t)} \mathbf{d}^*(\mathbf{k}) + \text{c.c.}, \tag{1.27}$$

where $\mathbf{d}(\mathbf{k}) = \langle \mathbf{k}|\mathbf{x}|0\rangle$ is the atomic dipole matrix element for the transition from the ground state to the continuum, $\boldsymbol{\kappa}_t = \mathbf{k} + \mathbf{A}(t)$ and $S(\boldsymbol{\kappa}_t, t', t)$ is the semiclassical action which represents the phase of the electron during the propagation in the continuum and is given by

$$S(\boldsymbol{\kappa}_t, t', t) = \int_{t'}^t dt'' \big(\frac{[\boldsymbol{\kappa}_t - \mathbf{A}(t'')]^2}{2} + I_p \big). \tag{1.28}$$

In conformity with the semiclassical model, Eq.(1.27) describes the same three steps as a sum of the product of their probability amplitudes. Here, $\mathbf{F}(t') \cdot \mathbf{d}(\boldsymbol{\kappa}_t - \mathbf{A}(t'))$ is

the transition probability amplitude from the ground state to the continuum at time of bith t'. The electron wavepacket propagates in the continuum in the time interval $t - t'$ as indicated by the factor $\exp(iS(\boldsymbol{\kappa}_t, t', t))$. Finally, the electron recombines with the amplitude $\mathbf{d^*}(\mathbf{k})$ at time t. The high harmonic spectrum can be calculated by obtaining the Fourier transform of $\mathbf{x}(t)$,

$$\mathbf{D}(\omega) = \int_{-\infty}^{\infty} dt e^{-i\omega t} \mathbf{x}(t). \tag{1.29}$$

Equation (1.29) is a triple integral over the variables $\mathbf{k}$, t', and t. The integral contains the product of a slowly varying oscillating function, $\mathbf{F}(t)$, and a faster one $\exp[i(S(\mathbf{k}, t', t) - \omega t)]$. The evaluation of the integral is analytically obtainable by using the *saddle-point* method [30]; it is based on taking advantage of the large oscillating function $\exp[i(S(\mathbf{k}, t', t) - \omega t)]$ and finding the points where it is stationary in terms of the three variables. Therefore, the three saddle points are

$$\nabla_{\mathbf{k}}(S - \omega t) = \int_{t'}^{t} dt'' v(t'') = \mathrm{x(t)} - \mathrm{x(t')} = 0 \tag{1.30a}$$

$$\frac{\partial}{\partial t'}(S - \omega t) = \frac{[\boldsymbol{\kappa}_t - \mathbf{A}(t')]^2}{2} + I_p = 0 \tag{1.30b}$$

$$\frac{\partial}{\partial t}(S - \omega t) = \frac{\mathbf{k}^2}{2} + I_p = \omega. \tag{1.30c}$$

Equation (1.30a) indicates that the displacement of an electron born at t' and returns at t is equal to zero. That means the electron returns to its specific parent ion. Intuitively, Eq. (1.30c) describes the energy conservation law, the left-hand side is the kinetic energy of the electron at the recombination time and the right-hand side is the energy of the $\mathrm{n^{th}}$ harmonic. Equation (1.30b) describes tunneling and determines the momentum of the electron evolving in the continuum after tunnel ionization. It says that the electron's kinetic energy at t' is negative, so its velocity $\boldsymbol{\kappa}_t - \mathbf{A}(t')$ is complex resulting in a complex tunnel time. The solution is given by $t' = t_b + i\delta t$, where t_b is determined by $\mathbf{k} = \mathbf{A}(t) - \mathbf{A}(t_b)$ in agreement with Eq. (1.21).

The three-step model agrees with the mechanism described by the classical model. If the electron is ionized in an appropriate time, it will be accelerated and then driven back to its parent ion. The recombination between the electron and the ion results in photon emission that is equal to the energy the electron gains during its excursion in the laser field.

1.3 Phase matching

It is worth pointing out that the dipole moment in Eq.(1.29) represents the single atom response which is not sufficient for describing the macroscopic harmonic yield. To obtain HHG signal from a macroscopic sample of atoms, propagation effects must be considered. Absorption plays a secondary role in atomic gases and is not further considered here.

For coherent harmonic emission, the phase difference between the input laser and the generated harmonics, Δk, must be zero. If the fundamental field and the harmonic field propagate at different phase velocities, the fundamental one will be out of phase with the harmonic field after a propagation distance known as *coherence length* and given be

$$L_{coh} = \frac{\pi}{\Delta k}. \tag{1.31}$$

Therefore, there will be a phase mismatch that lowers the harmonic efficiency. The dephasing for production the qth-harmonic order is expressed as

$$\Delta k = qk(\omega) - k(q\omega). \tag{1.32}$$

The following are a brief illustration of the main sources of the dephasing and some ways to control them. Precise explanation can be found in [41].

- Dispersion of the medium: Each harmonic is expected to propagate with a certain velocity that is different from other harmonics. This occurs because of the dependence of the refractive index on the frequency. On the other hand, the wavevector depends on the refractive index $n(\omega_0)$. This leads to a phase mismatch that is given by

$$\Delta k_{disp}(\omega_0) \propto qn(\omega_0) - n(q\omega_0). \tag{1.33}$$

- Plasma dispersion: At the final step of HHG, not all electrons recombine with their parent ions. Only a small percentage of the freed electrons do. The rest of the electrons fail to reach the core and become free for a time that is longer than the duration of the laser pulse. The resulting plasma frequency modifies the refractive index and so the wavevector leading to a negative contribution of the phase mismatch,

$$\Delta k_p(\omega_0) \propto \frac{\omega_p^2(1-q^2)}{2q\omega_0}, \tag{1.34}$$

  where $\omega_p = \sqrt{\frac{e^2 N_e}{\epsilon_0 m_e}}$ is the plasma resonance frequency with e, N_e, m_e, and ϵ_0 being the electron charge, the free-electron density, the electron mass, and the dielectric constant, respectively.

- Geometric dispersion: The geometric dispersion is classified based on the propagation environment, whether it is in free space or a guided beam. In free space, a Gaussian laser beam propagates along an optical axis with an intensity that is highly focused along the Rayleigh length. The beam intensity decreases over a longer propagation length. To keep the high intensity for a longer distance, propagation in a waveguide is used [42]. In both cases, there is an extra dephasing contribution that arises from Gouy phase shift in free space propagation (Δk_{foc}) and the dispersion of waveguided modes in guided beam propagation (Δk_{wg}). The two contributions can be approximated as

$$\Delta k_{geom}(\omega) \propto \begin{cases} 2(q-1) & \text{for free space, and} \\ (1-q^2) & \text{for waveguide.} \end{cases} \tag{1.35}$$

The total dephasing is represented by the sum of all contributions; therefore,

$$\Delta k \propto \begin{cases} n(\omega_0) - n(q\omega_0) + \frac{\omega_p^2(1-q^2)}{2q\omega_0} + 2(q-1) & \text{for free space, and} \\ n(\omega_0) - n(q\omega_0) + \frac{\omega_p^2(1-q^2)}{2q\omega_0} + (1-q^2) & \text{for wavegudied.} \end{cases} \tag{1.36}$$

The optimal HHG efficiency is achieved by minimizing Δk using a precise balance of these contributions. The difference of refractive indices at the fundamental laser frequency ω_0 and the qth-harmonic $q\omega_0$ is usually larger than one. That is because the typical frequency of the input laser in atomic HHG ranges from visible to near-IR, $n(\omega_0) > 1$, while $n(q\omega_0) < 1$ for XUV harmonic emission. Now, both Δk_{disp} and Δk_{foc} are positive while Δk_p is negative, so $\Delta k_{disp} + \Delta k_{foc} = \Delta k_p$ must be fulfilled to get $\Delta k = 0$. Some techniques to satisfy this condition include changing the position of the gas jet regarding the focus, changing the density of the gas, or changing the beam shape. However, methods to accomplish the phase matching in the case of the waveguided beam must consider that the geometric contribution now has the same negative sign as the plasma dispersion contribution. The most practical way to reduce the dephasing, in this case, is to change the gas density.

1.4 HHG tomography

There are many ways that attosecond pulses from HHG can be used to time resolve ultrafast processes in atoms and gases. The most prevalent schemes rely on a two-color pump-probe scenario with an ultrashort near-infrared laser pulse and an attosecond XUV pulse. However, as indicated in the introduction, HHG itself can be used as a probe for ultrafast and ultrafine processes. As an example I outline HHG spectroscopy in more detail, as it is relevant for the research done in my thesis.

In the limit $\gamma < 1$, the dipole moment given by Eq. (1.27) can be expressed as the product of three factors representing the three steps of the Lewenstein model [43]

$$\mathrm{x}(t) = Re\left[e^{-i\pi/4} \sum_{trajectories} a_I(t) a_P(t) a_R(t)\right] \tag{1.37}$$

with

$$\begin{aligned} a_I(t) &= \left(\frac{dn(t')}{dt}\right)^{1/2}, \\ a_P(t) &= \left(\frac{2\pi}{t-t'}\right)^{3/2} \frac{(2I_p)^{1/4}}{|F(t')|} e^{-i((t-t')I_p - iS(t))}, \text{and} \\ a_R(t) &= \sqrt{1-n(t_{rec})} \frac{A(t') - A(t)}{[2I_p + (A(t') - A(t))^2]^3}. \end{aligned} \tag{1.38}$$

where a_I, a_P, and a_R are the amplitudes of ionization, propagation and recombination, respectively. Here, $n(t') = 1 - \exp\left(-\int_{-\infty}^{t'} \mathrm{w(t')dt'}\right)$ is the probability of ionization with $\mathrm{w}(t')$ being the ionization rate, see Eq. (1.19). The probability amplitude $a_I(t)$ contributes to forming the amplitude spectrum due to its dependence on the ionization rate. The amplitude of propagation, $a_P(t)$, contains the factor $(t-t')^{-3/2}$ which describes the spreading of the wave packet in the continuum. Additionally, it has its effect on the phase due to the semiclassical action integral.

The harmonic spectrum is commonly calculated as the absolute square of the second time-derivative of $\mathbf{D}(\omega)$ given by Eq.(1.29) [44],

$$\tilde{I}(\omega) = \omega^4 \left| \int_{-\infty}^{\infty} e^{i\omega t} \mathbf{x}(t) dt \right|^2. \tag{1.39}$$

The dipole moment in the spectral domain can be then factorized into three amplitudes as

$$\tilde{I}(\omega) = \omega^4 \left| a(k) \mathbf{d}(\omega) \right|^2, \tag{1.40}$$

where the amplitudes of ionization and propagation have been combined into $a(k)$ while $\mathbf{d}(\omega) = \langle \Psi_0(\mathbf{x}) | \, \mathbf{x} \, | \mathbf{k} \rangle$ is the recombination dipole matrix elements with $|\Psi_0(\mathbf{x})\rangle$ being the ground state wavefunction. Here, the frequency-dependence of the amplitude a has been converted to k-dependence by using the Eq.(1.24). In the plane wave approximation, the recombination amplitude can be simplified to

$$\mathbf{d}(\omega) = \langle \Psi_0(\mathbf{x}) | \, \mathbf{x} \, | \mathbf{k} \rangle = \langle \Psi_0(\mathbf{x}) | \, \mathbf{x} \, | e^{i\mathbf{k}\cdot\mathbf{x}} \rangle. \tag{1.41}$$

Equation (1.41) is just the spatial Fourier transform of the ground state wavefunction. This form of the dipole allows reconstructing the ground state wavefunction by inverse Fourier transform, once the amplitude $a(k)$ has been factored out. In molecular gases this is done by comparing molecular harmonic spectra with harmonic spectra from well understood noble gases with the same ionization potential [25]. As a result of the same ionization potential, ionization and propagation are the same in both harmonic spectra and can be factored out from the molecular harmonic spectrum. This method has been used to time resolve chemical reactions and to tomographically measure the wavefunction of simple molecules [22–27].

Chapter 2

High harmonic generation in solids

Recently, the generation of high harmonic in the condensed matter phase has been developed. Ghimire et al. were the first who observed it when they illuminated a ZnO crystal using a mid-infrared laser pulse [8]. Other experiments depict HHG in semiconductors using THz [12–14] and mid-infrared [9–11] laser pulses. Vampa et al. have theoretically investigated HHG in bulk semiconductors and shown that HHG in semiconductor occurs via a three-step model similar to HHG in atoms [16]. In this chapter, HHG in bulk semiconductor is briefly reviewed.

2.1 Distinction from atoms

To understand the similarity and difference between HHG in atoms and semiconductors, it is more practical to describe the two processes in the momentum space. Figure 2.1 is a comparsion of the two models where the energy levels of an atom and the dispersion relation, $E(\mathbf{k})$, of a two-band solid are depicted. First, we must indicate that $\mathbf{k}$ is related to the momentum by $\mathbf{p} = \hbar\mathbf{k}$ in atomic case. In a solid $\mathbf{k}$ is the *crystal mometum* which is different to the classical momentum. It ranges from $-\pi/a$ to π/a where a is the lattice constant. The crystal momentum presents a good quantum number of solids reflecting the translation symmetry of solids.

In the strong laser-atom interaction, an electron in the ground state of the atom tunnels, gains the energy I_p and is born with zero velocity in the continuum. On the other hand, a crystal in k-space is described by two bands separated by an energy gap. The lower band is initially completely filled with electrons and called the *valence* band. The other band is practically empty and known as the *conduction*

band. In this case, the electron tunnels vertically from continuum states to another continuum in the presence of the strong laser field [37]. The electron leaves behind a vacant energy state in the valence band which is referred to as a *hole*. The hole motion must be considered since its mass is comparable to the electron mass. As a result of the negative and positive charges, electron and the hole are accelerated in different directions by the laser field. At a later time, the pair may reencounter, recombine and emit a photon. However, the energy of the emitted photon here is equal to the difference in energy between the conduction state and valence state at the moment of recombination. Another significant distinction from atoms is the non-parabolic band structure which is more pronounced towards the edges of the Brillouin zone (BZ). One can expect therefore that harmonic emission scales differently with laser intensity than in the atomic case.

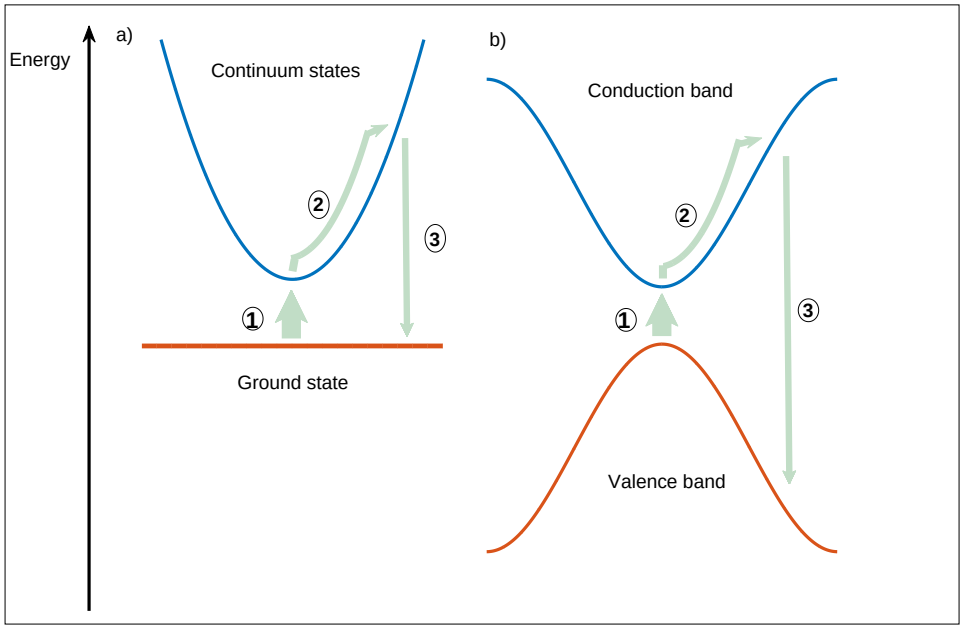

Figure 2.1: Diagram of the three-step model in the momentum space for (a) an atom (b) a bulk solid.

The evolution of classical particles in atomic case is described by Newton's equations, see Eqs. (1.20) to (1.23). In solids, the classical equations of motion are similar; however, the equation of motion is $d\mathbf{k}/dt = \mathbf{F}$ with $\mathbf{k}$ being the crystal momentum. Moreover, the velocity of the electron is the k-gradient of the energy

band in solids [45],

$$\mathrm{v}_m(\mathbf{k}) = \nabla_{\mathbf{k}} E_m(\mathbf{k}), \qquad m = v, c \tag{2.1}$$

where v and c signify valence and conduction bands, respectively. This results in limiting the velocity of the electron as it reaches the boundary of the Brillouin zone.

2.2 The nonlinearity of band velocity

There is a second mechanism that results in HHG in solids coming from the non-linearity of the band velocity. This mechanism does not exist in gases where the dispersion relation is purely quadratic and therefore the velocity is linear.

To illustrate how the velocity of electrons and holes results in harmonic emission, let us consider conduction and valence bands of a simple cubic lattice in the nearest neighbor approximation,

$$E_v(\mathrm{k}) = \quad \Delta_v\big(\cos(\mathrm{k}a) - 1\big) \tag{2.2a}$$

$$E_c(\mathrm{k}) = \; E_g + \Delta_c\big(1 - \cos(\mathrm{k}a)\big), \tag{2.2b}$$

where Δ_m represents the bandwidth and a is the lattice constant. Inserting Eqs. (2.2a) into Eq. (2.1) yields

$$\mathrm{v}_v(\mathrm{k}) = \; -a\Delta_v \sin(\mathrm{k}a), \tag{2.3a}$$

$$\mathrm{v}_c(\mathrm{k}) = \quad a\Delta_c \sin(\mathrm{k}a). \tag{2.3b}$$

When an electric field is applied, the crystal momentum is altered by the vector potential, $\mathrm{k} = \mathrm{A}(t)$ [45]. If the laser field is $F(t) = F_0 \cos(\omega_0 t)$, then the laser vector potential is $\mathrm{A}(t) = -(F_0/\omega_0)\sin(\omega_0 t)$ and the change of the crystal momentum is given by

$$\mathbf{k}(t) = \mathbf{k}_0 - \mathbf{A}(t), \tag{2.4}$$

where $\mathbf{k}_0$ is the free-field crystal momentum. Inserting this new crystal momentum into the conduction band velocity, Eq.(2.3a), yields [34]

$$\mathrm{v}_c(t) = -a\Delta_c \sin\left(\frac{aF_0}{\omega_0}\sin(\omega_0 t)\right). \tag{2.5}$$

Note we have assumed that the electron starts his motion at $\mathrm{k}_0 = 0$. Therefore, the velocity of an electron, that has already been excited to the conduction band due to the presence of the laser field, is a sinusoidal function in time. Clearly, the electron oscillates with the amplitude aF_0/ω_0. Taylor expansion of Eq. (2.5) shows immediately harmonic terms of the fundamental driving frequency. As the

amplitude of the electron oscillation exceeds the Brillouin zone boundaries, the electron reverses its direction due to the periodicity of the system. If the laser field is sufficiently high, the electron can undergo multiple reversals during one cycle. This phenomenon is known as *Bloch oscillations*. Figure. (2.2) shows the nonlinearity of the Bloch velocity of the electron in the conduction band. Increasing the laser field strength or its wavelength results in higher nonlinearity. However, the damage of the crystal limits the maximum useable intensity. [8].

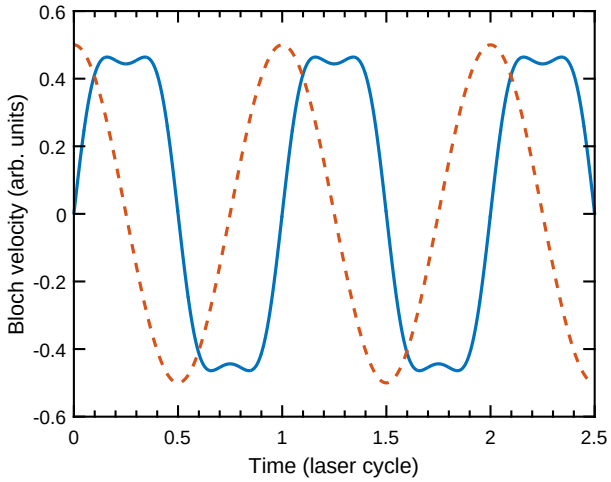

Figure 2.2: The Bloch velocity (blue) and the electric field (red).

The current due to this motion, known as *intraband current*, is given by [46],

$$\mathbf{j}_m(t) = \int_{BZ} \mathbf{v}_m(\mathbf{k}, t)\mathbf{n}_m(\mathbf{k}, t)d\mathbf{k}, \tag{2.6}$$

where the integral is over the first BZ and $\mathbf{n}_m(\mathbf{k}, t)$ is the number of electrons promoted to the conduction band. The spectrum is calculated by the absolute squared of the Fourier transform of the electron current.

2.3 Theory of HHG in solids

2.3.1 Solution of the time-dependent Schrödinger equation

The quantum description of HHG in solids can be obtained by solving the time-dependent Schrödinger equation (TDSE). In length gauge, the one-electron TDSE takes the form

$$i\partial_t \Psi(\mathbf{x}, t) = (H_0 - \mathbf{x}.\mathbf{F}(t))\Psi(\mathbf{x}, t), \tag{2.7}$$

where $H_0 = -\frac{1}{2}\nabla^2 + U(\mathbf{r})$ is the free field Hamiltonian with $U(\mathbf{r})$ being the periodic potential of the crystal. In the absence of the laser field the eigenfunctions $\Phi_{m,\mathbf{k}}$ fulfill $H_0\Phi_{m,\mathbf{k}} = E_m(\mathbf{k})\Phi_{m,\mathbf{k}}$ with $E_m(\mathbf{k})$ the band eigenenergies; further, $\Phi_{m,\mathbf{k}} = \frac{1}{\sqrt{V}}u_{m,\mathbf{k}}(\mathbf{x})\exp(i\mathbf{k}\cdot\mathbf{x})$ with $u_{m,\mathbf{k}}(\mathbf{x})$ the Bloch functions that are periodic with the lattice and V the volume of the solid [45]. One can make use of the periodicity of the potential and expand the wavefunction in a basis of Bloch states,

$$\Psi(\mathbf{x},t) = \int_{BZ} a_m(\mathbf{k},t)\Phi_{m,\mathbf{k}}(\mathbf{x})d^3\mathbf{k}, \tag{2.8}$$

where $a_m(\mathbf{k},t)$ is the probability amplitude. Substituting the wavefunction into Schrödinger equation results in equations of motion for the probability amplitudes,

$$\dot{a}_m(\mathbf{k},t) = \big(-iE_m(\mathbf{k}) + \mathbf{F}(t)\nabla_{\mathbf{k}}\big)a_m + i\mathbf{F}(t)\sum_{m'\neq m}\mathbf{d}_{mm'}(\mathbf{k})a_{m'}, \tag{2.9}$$

where

$$\mathbf{d}_{mm'} = \int_V u^*_{m,\mathbf{k}}(\mathbf{x})\nabla_{\mathbf{k}}u_{m',\mathbf{k}}(\mathbf{x})d^3\mathbf{x} \tag{2.10}$$

is the transition dipole moment between the two bands. Equation (2.9) shows the following contributions. The term that contains $\nabla_{\mathbf{k}}$ drives the eletron/hole along their respective bands. This current is the intraband current. The third term represents the dipole transition between the two bands.

Using the variable transformations: $b_m = a_m\exp\Big(i\int_{-\infty}^{t}E_m(\boldsymbol{\kappa}+A(t')dt')\Big)$, one can obtain

$$\begin{aligned}\dot{b}_{c,\kappa} &= i\mathbf{F}\cdot\mathbf{d}^*_{c,v}(\mathbf{k})b_{v,\kappa}\exp[iS(\boldsymbol{\kappa},t)]\\ \dot{b}_{v,\kappa} &= i\mathbf{F}\cdot\mathbf{d}_{v,c}(\mathbf{k})b_{c,\kappa}\exp[-iS(\boldsymbol{\kappa},t)]\end{aligned} \tag{2.11}$$

where $S(\boldsymbol{\kappa},t) = \int_{-\infty}^{t}\varepsilon_g\big(\boldsymbol{\kappa}+A(t')\big)dt''$ is the classical action with $\varepsilon_g = E_c - E_v$ being the energy gap. The transition dipole moment $\mathbf{d}_{m,m'}$ is given by Eq. (2.10). The crystal momentum $\mathbf{k} = \boldsymbol{\kappa} + \mathbf{A}(t)$ has been transformed into a frame moving with the vector potential; this transformation also results in a transformation of the Brillouin zone $\overline{\mathrm{BZ}} = \mathrm{BZ} - \mathbf{A}(t)$. Eqs.(2.11) are integrated numerically by using a fourth-order Runge-Kutta method, see Appendix C.

In solids, scattering from other electrons, ions, or phonons plays an important role. These dephasing mechanisms can be taken into account by including dephasing time in the probability amplitude equations, Eqs. (2.11). For this purpose, it is easier to deal with the density matrix approach [47] which deals with band populations ($n_m = |b_m|^2$) and coherence ($\pi = b_m b_{m'}$) instead of the probability amplitudes.

The main advantage of using the density matrix approach is the potential to include dephasing phenomenologically. Vampa et al. employed the density matrix approach to derive the HHG currents and investigate the effect of the dephasing [10,16,17,48].

The current of HHG in the density matrix approach is given by the two contributions:

$$\mathbf{j}_{er}(t) = \frac{d}{dt}\int_{\overline{BZ}} \mathbf{p}(\boldsymbol{\kappa}, t) d^3\boldsymbol{\kappa} \tag{2.12a}$$

$$\mathbf{j}_{ra}(t) = \sum_m \int_{\overline{BZ}} \mathbf{v}_m(\boldsymbol{\kappa} + \boldsymbol{A}(t)) n_m(\boldsymbol{\kappa}, t) d^3\boldsymbol{\kappa}, \tag{2.12b}$$

where

$$\mathbf{p}(\boldsymbol{\kappa}, t) = \mathbf{d}(\boldsymbol{\kappa}, t)\pi(\boldsymbol{\kappa}, t)\exp(iS(\boldsymbol{\kappa}, t)) + \text{c.c.} \tag{2.13}$$

is the polarization due to dipole transitions. Here, $\mathbf{j}_{ra}(t)$ is the current due to the motion of carriers with nonlinear velocity in each band and $\mathbf{j}_{er}(t)$ is due to the polarization between the two carriers in the two different bands. The equations of motion for band population and polarization representing the coherence between the two bands are given by

$$\dot{\pi}(\boldsymbol{\kappa}, t) = -\frac{\pi(\boldsymbol{\kappa}, t)}{T_2} + i\mathbf{F}\cdot\mathbf{d}(\boldsymbol{\kappa} + \mathbf{A}(t))\delta_n e^{iS(\boldsymbol{\kappa}, t)}, \tag{2.14a}$$

$$\dot{n_m}(\boldsymbol{\kappa}, t) = i\sigma_m \mathbf{F}\cdot\mathbf{d}(\boldsymbol{\kappa} + \mathbf{A}(t))\pi e^{-iS(\boldsymbol{\kappa}, t)} + \text{c.c.} \tag{2.14b}$$

The parameter T_2 is phenomenologically introduced which is the dephasing time that damps coherences between the two bands. Here, $\delta_n = n_c - n_v$ is the band population difference, and $\sigma_m = -1, 1$ for $m = v, c$, respectively.

Finally, the *intraband* and *interband* currents are calculated as the absolute square of Fourier transform of Eqs. (2.12),

$$\begin{aligned}\mathbf{j}_{ra}(\omega) = \omega \int_{-\infty}^{\infty} dt e^{-i\omega t}\Bigg[\int_{BZ} d^3\boldsymbol{k}\mathbf{v}_m(\boldsymbol{k}) \int_{-\infty}^{t} dt' F(t') d^*(\kappa(t')) \times \\ \int_{-\infty}^{t} dt'' F(t'') d^*(\kappa(t;')) \times \\ \exp\{iS(\boldsymbol{k}, t'', t') - (t' - t'')/T_2\} + \text{c.c.}\Bigg],\end{aligned} \tag{2.15}$$

$$\mathbf{j}_{er}(\omega) = \omega \int_{-\infty}^{\infty} dt e^{-i\omega t} \Bigg[\int_{BZ} d^3\boldsymbol{k} d^*(\boldsymbol{k}) \int_{-\infty}^{t} dt' F(t') d(\kappa(t')) \times \exp\{iS(\boldsymbol{k}, t', t) - (t - t')/T_2\} + \text{c.c.} \Bigg] \tag{2.16}$$

HHG spectra for intra- and interband currents are shown in Figure 2.3. Clearly, the intraband harmonics prevail in the perturbative region while the interband contribution is dominant in the non-perturbative region.

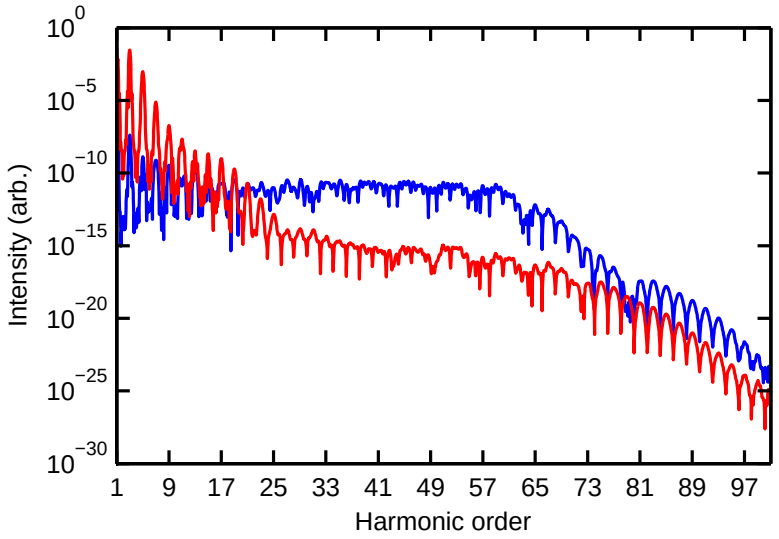

Figure 2.3: Harmonic spectra for the interband (blue) and intraband (red) contributions in 1D semiconductor with $E_g = 3.3\,\text{eV}$ and $T_2 = 1\,\text{fs}$. The band structure is given by Eqs. (3.2). The system is exposed to a Gaussian pulse of $\lambda_0 = 6.4\,\mu\text{m}$ at $F_0 = 0.26\,\text{V}\cdot\text{Å}^{-1}$ with a FWHM of three cycles.

Now, the question of where the plateau in the interband spectrum comes from needs to be answered. Hence, the three-step model is used to explain the physics behind the presence of plateau.

2.3.2 Semiclassical model for semiconductor HHG

The approximate solution of the integrals on Eq. (2.16) is given by utilizing the saddle point method. It is logical to use this method since the integral includes the multiplication of a slow oscillating function, the laser field, with a faster one, the classical action. The three saddle points are obtained by taking the first derivatives of the classical action with regard to the three integration variables. This results in

$$\nabla_{\mathbf{k}} S = = \Delta \mathrm{x_m} - \Delta \mathrm{x_{m'}} = 0 \tag{2.17a}$$

$$\frac{\partial S}{\partial t'} = \varepsilon_g[\boldsymbol{\kappa} + \boldsymbol{A}(t')] = 0 \tag{2.17b}$$

$$\frac{\partial S}{\partial t} = \varepsilon_g(\mathbf{k}) = \omega \tag{2.17c}$$

where $\Delta \mathrm{x_m} = \int_{\mathrm{t'}}^{\mathrm{t}} \mathrm{v_m(t'')dt''} = \mathrm{x_m(t)} - \Delta \mathrm{x_m(t')}$, t' is the time of electron (hole) birth from $m = c$ ($m = v$), and t represents the time of observation. Equation (2.17a) indicates that the electron (hole) that leaves the conduction (valance) band at time t' returns to the same position after a duration $\tau = t - t'$. Equation (2.17b) states that the energy gap at the point $\boldsymbol{\kappa} + \boldsymbol{A}(t')$ at the time of birth must be equal to zero; however, the minimum value of $\varepsilon_g(\mathbf{k}) > 0$. Therefore, the parameter $\boldsymbol{\kappa} + \boldsymbol{A}(t')$ must be complex, so its imaginary part describes tunneling and its real part describes propagation of the pair. The real part then is

$$\mathbf{k} = \boldsymbol{A}(t) + \boldsymbol{A}(t') = 0. \tag{2.18}$$

Equation (2.18) implies that an electron and a hole born at t' at the Γ point are accelerated by the laser field in the k space. The equation of stationary point t, Eq.(2.17c), shows that the energy is conserved; the recombination of the pair results in emitting a photon with energy ω that is equivalent to the energy gap at the recombination moment.

In general, the physics of the three-step model in solids is very similar to that in atoms, see Eqs.(1.30).

2.3.3 Effect of dephasing on interband vs intraband harmonics

As we stated above, the scattering of electrons with other particles can be represented phenomenologically by dephasing. The coherence between electrons and holes is lost on the scale of T_2. If T_2 is comparable to the laser pulse duration, then there is enough time to have multiple recollisions. The interference of photons emitted during different half cycles results in a noisy spectrum. By contrast, if the dephasing time is comparable to the laser cycle, recollisions are suppressed and some of the electrons never return. Short decoherence times affect the interband and intraband contributions to HHG differently. As such, there is the possibility that a small value of T_2 may suppress the interband contribution enough, particularly at longer wavelengths, so that the intraband contribution becomes the dominant contributor to HHG.

This has been examined in Fig. 2.3. The dephasing time T_2 is introduced into our two-band system as was done in Ref. [16]. We solve the two-band equations for our 1D model solid with $E_g = 3.3\,\mathrm{eV}$, $\lambda_0 = 6.4\,\mu\mathrm{m}$, $F_0 = 0.26\,\mathrm{V{\cdot}\AA^{-1}}$ and $T_2 = 1\,\mathrm{fs}$. This particular set of parameters represents an extreme case, as the dephasing time is $1/20^{\mathrm{th}}$ of the optical cycle. Still, Figure 2.3 shows that interband HHG (blue) remains dominant over intraband HHG (red).

Chapter 3

HHG in Low-Dimensional Solid State Systems

Here, we theoretically investigate the effect of quantum confinement on high harmonic generation in semiconductor materials. The main idea is the study of strong field dynamics in nanostructures. The backbone of our investigation is the study of the effect of varying width of nanostructure on ionization and HHG. The effects that quantum confinement has on harmonic generation output are presented in this chapter. The quantum confinement is performed by varying the width of a model nanostructures. Our analysis reveals a reduction in ionization and a concurrent growth in HHG efficiency with increasing confinement. The drop in ionization results from an increase in the bandgap due to stronger confinement. The increase in harmonic efficiency comes as a result of the confinement restricting the spreading of the transverse wavepacket. As a result, intense laser driven 1D and 2D nanosystems present a potential pathway towards scaling HHG to higher efficiencies and photon energies.

3.1 Quantum confinement

A confined quantum system is defined as a low-dimensional system where the motion of the carriers (electron and hole) are restricted to a length scale that is comparable to the electron wavelength in one or more directions. Based on the confinement direction, a quantum confined structure will be classified into three types: quantum well (one direction), quantum wire (two directions) and quantum dots (three directions), where the parentheses represent the number of confinement directions.

A quantum well; for example, can be formed by a thin layer of a narrower-

bandgap material that is surrounded by two layers of a wider-bandgap material. The middle layer must be sufficiently thin for quantum properties to be exhibited. For our purpose in this chapter, the width of this layer should be comparable to the unit cell. Because of the difference in Fermi levels, carriers are trapped in the well. Thus, electron and hole are localized in the same region of space, which makes for efficient recombination.

For any of the three structures, the electron momentum is quantized in the confinement direction. Therefore, the energy along this direction will be limited to a series of discrete values. Along these directions, the continuous energy bands of bulk material are not valid anymore. In addition, the confinement of particles within a small distance leads to an increase in their momentum and energy. This band structure directly impacts the electronic and optical properties of the material which makes these structures efficient in several applications and devices. Nanostructures and its applications have been extensively studied and illustrated in several textbooks, see for example [49].

3.2 Quantum confinement role in enhancing HHG

Quantum diffusion is one of the limitations of HHG, in the gas as well as the condensed matter phase. It increases the transverse wavepacket width during propagation and therewith reduces the recombination probability. Therefore, this results in reducing the intensity of the harmonic output. In the atomic case, confining the system transversely with a magnetic field can be used to counteract quantum diffusion and to increase HHG [21].

In solid state systems, quantum diffusion also plays a similar role in the recollision process. This impacts the efficiency of interband HHG [15, 16]. Figure 3.1 shows a schematic depiction of this process; here the k-space formalism has been transformed into the Wannier picture where the electron/hole wavefunctions are localized in space. When an electron-hole pair is created, they are propagated in the field. During this propagation, the wave packet spreads leading to a reduction in the recollision cross-section and thus lower harmonic output. In the bulk case where there is no confinement, the spreading of the wave packet in space results from the time-dependent phase contribution from the transverse crystal momentum distribution; see equation (A.28) for an approximate solution. Here the spreading of the wave packet will be maximally resulting in a reduction in the recollision cross-section and thus lowering the harmonic output; see Fig. 3.1(a). By contrast, when the confinement is such that there is only a single transverse state, spreading of the wave packet will be reduced, or eliminated altogether, resulting in a higher

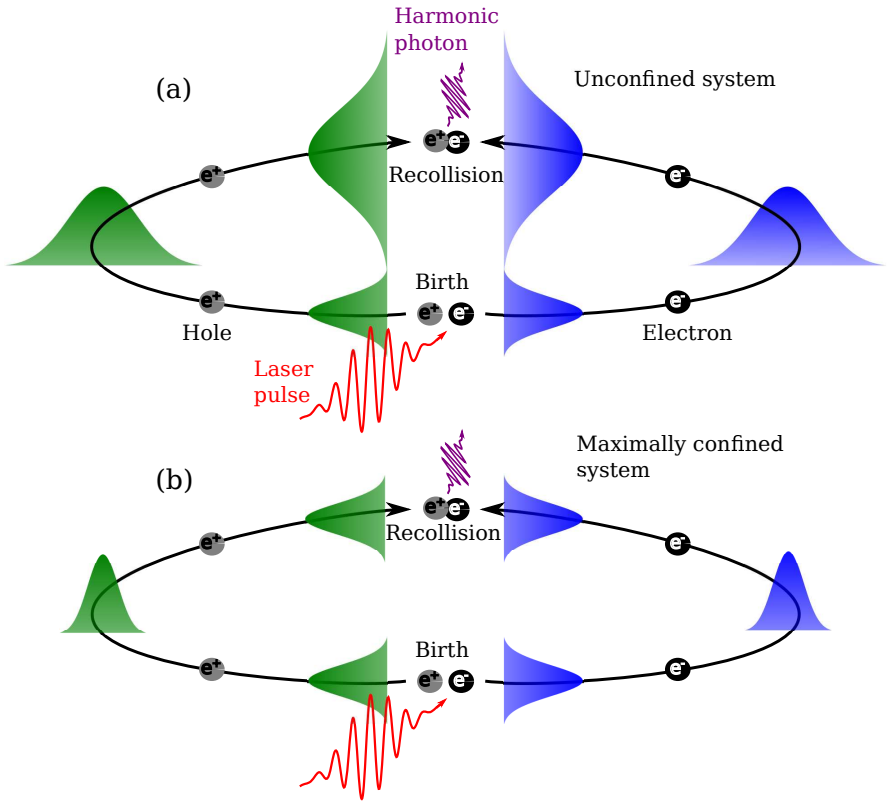

Figure 3.1: Schematic depiction of the effect of quantum confinement on wave packet spreading and interband harmonics; the black circles represent electrons and the grey circles represent holes. Here the k-space formalism has been transformed into the Wannier picture.(a) In the bulk solid there is no transversal confinement. When an electron-hole pair is created by the laser field, their wave packets have an initial width. As the electron-hole pair is propagated in time (depicted by the black curved arrows) by the field, their wave packets begin to spread. The spreading behavior results from the time-dependent phase from the k-space distribution in the transverse direction; see equation (A.28). At the time of recollision, the wave packets will have undergone significant spreading thus reducing their harmonic output. (b) When the system is maximally confined (this would correspond to a one-dimensional system containing only a single transverse state) the wave packet is unable to spread during propagation in the field. Thus, at the time of recollision, maximal overlap will occur, resulting in an enhanced harmonic efficiency.

ionization probability; see Fig. 3.1(b).

3.3 Methods

3.3.1 Model for confined quantum systems

Our model of the confined systems consists of a single valence band (v) and a single conduction band (c). It has been noted that multiple bands need to be considered when the system experiences significant Bloch oscillation [50] or when multiple harmonic plateaus are of interest [51]. For the field strengths used here, Bloch oscillations are not a significant concern. Further, parameters that are used for our model semiconductor are similar to those used in reference [51] where it was shown that the first plateau in the harmonic spectrum determined by the two band system did not differ significantly to that of the corresponding 51 band system.

The valence and conduction bands in our model can be expressed as $E_m = \sum_j E_{m,j}$ where $j = x, y, z$ and $m = c, v$. The $\hat{z}$ direction is chosen to be longitudinal to the laser field. The band gap along each confined transverse direction is determined by a periodic potential $v(u)$ ($u = x, y$). For a single lattice site of width a_u and well of depth v_0 this is given by,

$$v(u) = \begin{cases} v_0 e^{-\frac{u^2}{\sigma_u^2 - u^2}} & \text{for } 0 \leq u < \sigma_u \\ v_0 e^{-\frac{(u-a_u)^2}{\sigma_u^2 - (u-a_u)^2}} & \text{for } a_u - \sigma_u < u \leq a_u \\ 0 & \text{otherwise} \end{cases} \tag{3.1}$$

where $\sigma_u = 0.41$Å. The width along the direction of confinement L_u is determined by choosing the number of lattice sites. The resulting one-dimensional Hamiltonians are then diagonalized numerically. When confinement is along both transverse directions we choose equal confinement widths along both directions and denote this width by $L = L_x = L_y$. When confinement is along a single direction we will designate this as the transverse $\hat{x}$ direction. In these systems we have $L = L_x$ and we fix $L_y = 50\,\text{nm}$. When $L = 50\,\text{nm}$ the band structure is nearly identical to that of the bulk crystal.

We express the band gap for the confined system as $\varepsilon_L(\mathbf{k}) = \overline{\varepsilon}_L(\mathbf{n}_\perp) + \varepsilon_\parallel(k_\parallel)$ where $\overline{\varepsilon}_L(\mathbf{n}_\perp) = E_g + \varepsilon_\perp(\mathbf{n}_\perp, L)$ and $\varepsilon_\perp$ and $\varepsilon_\parallel$ are band gaps in the transverse and longitudinal directions to the field; E_g is the minimum band gap of the bulk crystal. The transverse confinement causes the band structure to form a discrete set of states. As such, here we define $\mathbf{k} = (\mathbf{n}_\perp, k_\parallel)$ with $\mathbf{n}_\perp = (n_x, n_y)$ being the quantum numbers of the transverse states and $k_\parallel = k_z$ being the longitudinal crystal momentum. The minimum band gap energy of the confined system is denoted by

Table 3.1: Fourier coefficients for the valence and conduction bands of our direct band gap semiconductor along the $\hat{z}$ direction [17]. The parameters are for the $\Gamma-$M band of ZnO.

Index	α_j (eV)	β_j(eV)
0	-2.5242	2.4426
1	1.9176	-2.2141
2	0.5440	-0.0653
3	-0.0326	-0.1306
4	0.0789	-0.0082
5	0.0163	-0.0245

$E_L = \bar{\varepsilon}_L(1,1)$ with $n_x = n_y = 1$ being the lowest transverse level. Further, we denote the bandwidth of our model system as $\Delta_L = \max[\varepsilon_L(\mathbf{k})]$, the maximum difference between the lowest valence and the highest conduction bands. Finally, when discussing the bulk material along the transverse direction, we will drop the L label and replace $\mathbf{n}_\perp$ with $\mathbf{k}_\perp = (k_x, k_y)$ the usual crystal momentum. Note that the notation above does not explicitly differentiate between systems confined along a single direction and those confined along both transverse directions. However, it is implied that when discussing confinement along both transverse directions, the L-label refers to the width of confinement along each of these directions, whereas, when discussing confinement along a single direction, the L-label only refers to confinement along the $\hat{x}$ direction.

The longitudinal band gap $\varepsilon_\parallel$ is unaffected by the confinement. This can be expressed by a Fourier cosine expansion,

$$E_{v,z}(k_z) = \sum_{j=0}^{5} \alpha_j \cos(jk_z a_z) \tag{3.2a}$$

$$E_{c,z}(k_z) = E_g + \sum_{j=0}^{5} \beta_j \cos(jk_z a_z) \tag{3.2b}$$

where $\varepsilon_\parallel = E_{c,z} - E_{v,z}$ with E_g being the minimum band gap and a_z the lattice spacing along the $\hat{z}$ direction. The band coefficients α_j and β_j are given in Table 3.1 and the band structure is shown in Fig. 3.2(a). The dipole parallel to the longitudinal direction is given by $d_z(\mathbf{k}) = \sqrt{E_{p,z}/(2\varepsilon_\parallel^2(k))}$ where $E_{p,z}$ is the Kane parameter [52–55]; here we use $E_{p,z} = 0.3$ a.u.

In our calculations we use $E_g = 3.3\,\text{eV}$ as the minimum band gap in the bulk crystal. The lattice periodicity and effective mass are $a_z = 2.8$Å and $m_z = 0.098m_e$.

Along the transverse directions the wells have a depth of $v_0 = 13.6\,\text{eV}$ and a lattice spacing of $a = a_{x,y} = 5\text{Å}$. In the bulk limit the effective transverse mass is $m_{x,y} = 0.053m_e$; Fig. 3.2(b) shows the transverse band gap in this limit. As a result of the quantum confinement, the transverse band structure is arranged into discrete levels; this is demonstrated for $L = 2\,\text{nm}$ in Fig. 3.2(c). Further, confinement increases the band gap as the confinement becomes narrower; this behavior is shown in Fig. 3.2(d). Our calculations consider confinement widths in the range from $L = 50\,\text{nm}$, where the band structure is very close to that of the bulk, down to $L = 1\,\text{nm}$ where there are only two atomic sites along each confined transverse direction.

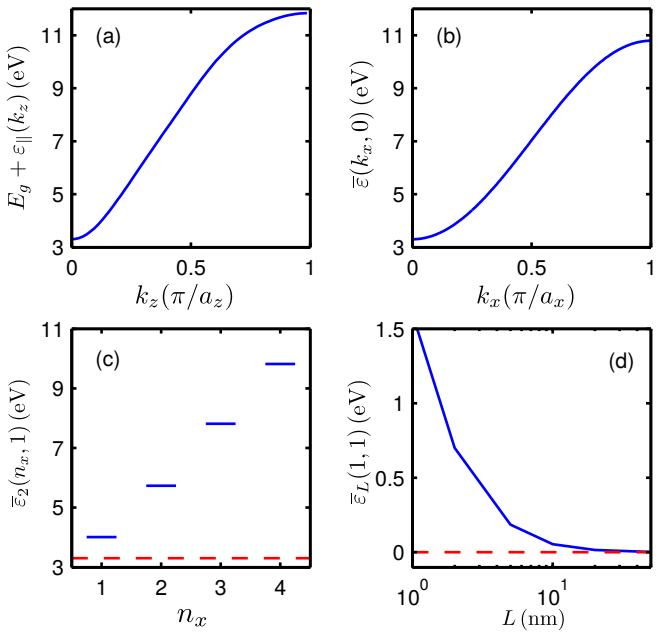

Figure 3.2: (a) Band gap along the longitudinal and (b) transverse x-direction for the bulk crystal. (c) Band gap along the transverse x-direction for a single confined direction with $L = 2$ nm. (d) Increase in band gap energy resulting from confinement along a single transverse axis; the dashed lines in (c) and (d) represent the bulk limit.

3.3.2 Ionization dynamics and high harmonic generation

In our analysis of ionization and HHG, we employ the frozen valence band approximation [56]. Here it is assumed that the valance band population remains largely unchanged as a result of the interaction between the solid and laser. With the frozen valence band approximation, the population transferred from valence to the

conduction band can be expressed through,

$$n_c(t) = \mathcal{N} \int_{\overline{BZ}} \left| \int_{-\infty}^{t} dt' \Omega^*(\mathbf{K}, t') e^{iS(\mathbf{K},t')} \right|^2 d^3\mathrm{K}, \tag{3.3}$$

where

$$S(\mathbf{K}, t) = \int_{-\infty}^{t} \varepsilon_L\big(\mathbf{K} + \mathbf{A}(t')\big) dt'. \tag{3.4}$$

is analogous to the classical action with $\mathbf{A}(t)$ being the vector potential. The crystal momentum $\mathbf{k} = \mathbf{K} + \mathbf{A}(t)$ has been transformed into a frame moving with the vector potential; this transformation also results in a transformation of the Brillouin zone $\overline{\mathrm{BZ}} = \mathrm{BZ} - \mathbf{A}(t)$. Further, $\Omega(\mathbf{K}, t) = \mathbf{d}\big(\mathbf{K} + \mathbf{A}(t)\big) \cdot \mathbf{F}(t)$ is the time-dependent Rabi frequency with $\mathbf{d}$ the dipole transition moment. The electric field is determined through $\mathbf{F}(t) = -d\mathbf{A}/dt$ and $\mathcal{N}$ is a constant that ensures normalization of the initial valence band population. When performing our calculations, we will be interested in the final conduction band population versus the width of the confinement L; we will denote this quantity as $n_c(L) = n_c(L, t = \infty)$. The dependence on L enters through the band structure ε_L in $S(\mathbf{K}, t)$. Finally, our wavefunction is normalized to unity for each L to ensure an equivalent amount of material is considered when comparing different L's. What this means is that when confinement is along two transverse directions, four objects of width $L/2$ are compared with a single object of width L or, in the case of confinement along a single direction, two objects with confinement width $L/2$ are compared with a single object with confinement L.

As mentioned above, high harmonic generation in solids can be produced from two currents — an interband current and an intraband current. The interband term was demonstrated to be the dominant contributor to above band gap harmonics generated in semiconductors exposed to a mid-infrared laser field [10, 16]. As such, we will focus on the interband term. It has been verified that the intraband term produces harmonics, in the above bandgap range, that are several orders of magnitude less intense than those produced by the interband term, thus rendering it negligible for the cases considered in this work. We do note, however, that when dephasing is strong or THz fields are used, the intraband harmonics may become a significant contributor to HHG [13, 16]. In Sec. 2.3.3, we have demonstrated that even for a short decoherence time the interband contribution is dominant in the above bandgap range for the longest wavelength considered in our calculations.

In the frozen valence band approximation [56], the interband current in frequency

space can be written as [16],

$$\mathbf{j}(\omega) = \mathcal{N}\omega \int_{\overline{BZ}} d^3\mathbf{K} \int_{-\infty}^{\infty} dt e^{-i\omega t} \mathbf{d}^*\big(\mathbf{K} + \mathbf{A}(t)\big) \times \int_{-\infty}^{t} dt' \Omega(\mathbf{K}, t') e^{iS(\mathbf{K},t,t')} + \text{c.c.}, \tag{3.5}$$

where $S(\mathbf{K}, t, t') = \int_{t'}^{t} \varepsilon\Big(\mathbf{K} + \mathbf{A}(t'')\Big) dt''$. The harmonic spectrum is determined by taking the magnitude square of equation (3.5). As a measure of the harmonic efficiency, we define the harmonic yield Φ as,

$$\Phi(L) = \int_{E_L}^{E_L + \Delta_L} \big|\mathbf{j}(\omega)\big|^2 d\omega. \tag{3.6}$$

Hence, $\Phi(L)$ is the total contribution of the allowed above band gap harmonics; see the inset of Fig. 3.3(d). Finally, we define the yield ratio as $\Phi(L)/n_c(L)$. This gives a measure of the harmonic yield per ionization event.

The quantum confinement results in two phenomena — an increase of the band gap and a reduction in the density of transverse states. Both effects will have influence on ionization and HHG. The band gap increase will result in lower ionization and, consequently, a reduced harmonic output. In contrast, the reduction of the density of transverse states will restrict the spreading of the quantum wave packet. This will result in an increase of recollision cross section and therewith an increase in HHG. By varying L alone, these contributions will remain coupled. In order to quantify these two contributions, it is necessary to separate them. This is can be achieved by noting that the ultimate limit of confinement occurs when there is only a single atom along each confined direction. In the case of the nanowire, the system becomes an atomic chain and in the case of the quantum sheet, the system becomes a monolayer. By neglecting the transverse coordinates of a 3D bulk material, the band gap of the resulting 1D and 2D mediums remains unchanged. However, the system has now gone from no confinement to a maximally confined system. Thus, by comparing the 3D bulk material to its corresponding 1D and 2D limits, we will be able to isolate the effect resulting from the spreading of the wave packet.

Additionally, we can gain insight by comparing the 3D bulk to its 1D and 2D limits through an analytical expression. This can be achieved for both ionization and HHG, as both can be represented as a product of the confined and non-confined contributions. Following the approach of Keldysh/Lewenstein [30, 37], saddle point integration of equation (3.3) followed by integration over the confined transverse

momentum coordinates can be achieved. The conduction band population can be written as the product $n_c = n_c^{(3-q)D} n_\perp^{qD}$ where, $n_c^{(3-q)D}$ is the contribution from the longitudinal and unconfined transverse coordinates and $n_\perp^{qD}$ is the confined transverse coordinate contribution. The quantity q indicates the number of confined transverse coordinates; for the remainder of this work we will use $q = 2$ to denote confinement along both transverse directions and $q = 1$ for confinement along a single transverse direction. The contribution coming from the confined transverse direction(s) can then be written as,

$$n_\perp^{qD} = \left(\frac{F_0^2}{2m_z E_g}\right)^{q/4} \prod_{j=1}^{q} a_j \sqrt{\frac{m_j}{2\pi}}, \tag{3.7}$$

where $j = 1, 2$ has been substituted for $j = x, y$; for a complete derivation of equation (3.7), see Appendix A. Similarly, by applying saddle point integration to equation (3.5), the 3D current j_{3D} can also be split into an unconfined current term $j_{(3-q)D}$ and a confined transverse term $j_\perp^{qD}$ where,

$$|j_\perp^{qD}|^2 = \left(\frac{2m_z E_g}{F_0^2} + \frac{\pi^2}{\omega_0^2}\right)^{-q/2} \prod_{j=1}^{q} a_j m_j. \tag{3.8}$$

In equation (3.8), j and q have the same meaning as in equation (3.7); as with equation (3.7), a derivation of equation (3.8) is provided in Appendix A. Note that equations (3.7) and (3.8) scale differently with the transverse effective masses m_j. Consequently, HHG will be affected more strongly by a change in the effective mass of the electron-hole pairs when a different material is used, than will ionization. Finally, for the above expression to be valid, the Keldysh parameter must satisfy $\gamma < 1$; all calculations presented here have $0.22 < \gamma < 0.87$.

3.4 Results and Discussion

3.4.1 Ionization and harmonic output

Our confined quantum systems are exposed to an intense laser-field having vector potential $\mathbf{A}(t) = \hat{z}(F_0/\omega_0) f(t) \cos(\omega_0 t)$ where ω_0 is the driving laser frequency corresponding to a central wavelength of λ_0; the pulse envelope $f(t)$ is Gaussian with a FWHM of three cycles. The peak field strength is $F_0 = 0.26\,\mathrm{V{\cdot}\AA^{-1}}$; this corresponds to a peak field intensity of $I_0 = 8.8 \times 10^{11}\,\mathrm{W{\cdot}cm^{-2}}$. In Fig. 3.3 the top four panels (a)-(d) present results for our model system with confinement along both transverse directions ($q = 2$); the bottom four panels (e)-(h) show our results when confinement is only along a single transverse direction ($q = 1$). Figures 3.3(a)

and 3.3(e) show the time-dependence of the population in the conduction band for $L = 50\,\text{nm}$ (blue) and $L = 1\,\text{nm}$ (red) with a driving wavelength of $\lambda_0 = 6.4\,\mu\text{m}$. The final conduction band population versus confinement width is plotted in Figs. 3.3(b) and 3.3(f). For $L = 50\,\text{nm}$ ionization has reached a plateau and is near to that of the bulk crystal. As the confinement width is decreased to 1 nm, there is a significant decrease in the final conduction band population. This decline in the final population is much more drastic when both transverse directions are confined. In the case where $q = 2$ (Fig. 3.3(b)) the drop is by several orders of magnitude, whereas, for $q = 1$ (Fig. 3.3(f)) the drop is just over an order of magnitude.

In both cases, this behaviour can be attributed to the increase in the band gap that results from the quantum confinement. Since this increase in band gap is larger for when $q = 2$ — due to the confinement of both transverse directions — a nanowire will experience a suppression of ionization that is greater than that of a thin slab where confinement is restricted to a single transverse direction. For the few-cycle pulses used here, optical field ionization is the primary mechanism leading to material damage; other ionization channels, such as collisional ionization, are of sub-ordinate importance. Damage occurs once the conduction band population reaches the percent level. As a result, from Figs. 3.3(b) and 3.3(e) it follows that the damage threshold intensity increases with stronger confinement; that is with decreasing L.

Further, in accordance with experiments on semiconductors [57], the time dynamics of the conduction band population for $L = 50\,\text{nm}$ displays a growth that is with the laser half-cycle. By contrast, the $L = 1\,\text{nm}$ results display mainly transient population dynamics with a small carrier density remaining after the pulse, similar to that observed in dielectric experiments [58]. This opens the possibility to nano-engineer semiconductor materials to be used in PHz optoelectronics where so far the primary candidates are dielectrics [58–60] or graphene [61].

Figure 3.3(c) shows the harmonic spectra for the $q = 2$ system with $L = 50\,\text{nm}$ (blue) and $L = 1\,\text{nm}$ (red) at $\lambda_0 = 6.4\,\mu\text{m}$. The shaded region shows the above band gap range $[E_L, E_L + \Delta_L]$ — over which integration in equation (3.6) is performed — for the $L = 50\,\text{nm}$ system. The spectrum for the 1 nm confinement is shifted due to the increase in band gap, and thus, the region of integration is shifted accordingly. Figure 3.3(d) displays the harmonic yield determined from equation (3.6) for the $q = 2$ system. The results for the $q = 1$ system, corresponding to Figs. 3.3(c) and 3.3(d), are presented in Figs. 3.3(g) and 3.3(h). When comparing Figs. 3.3(c) and 3.3(g), it can be seen that the increase in harmonic intensity for $L = 1\,\text{nm}$ is much more pronounced when both transverse directions are confined. This behaviour

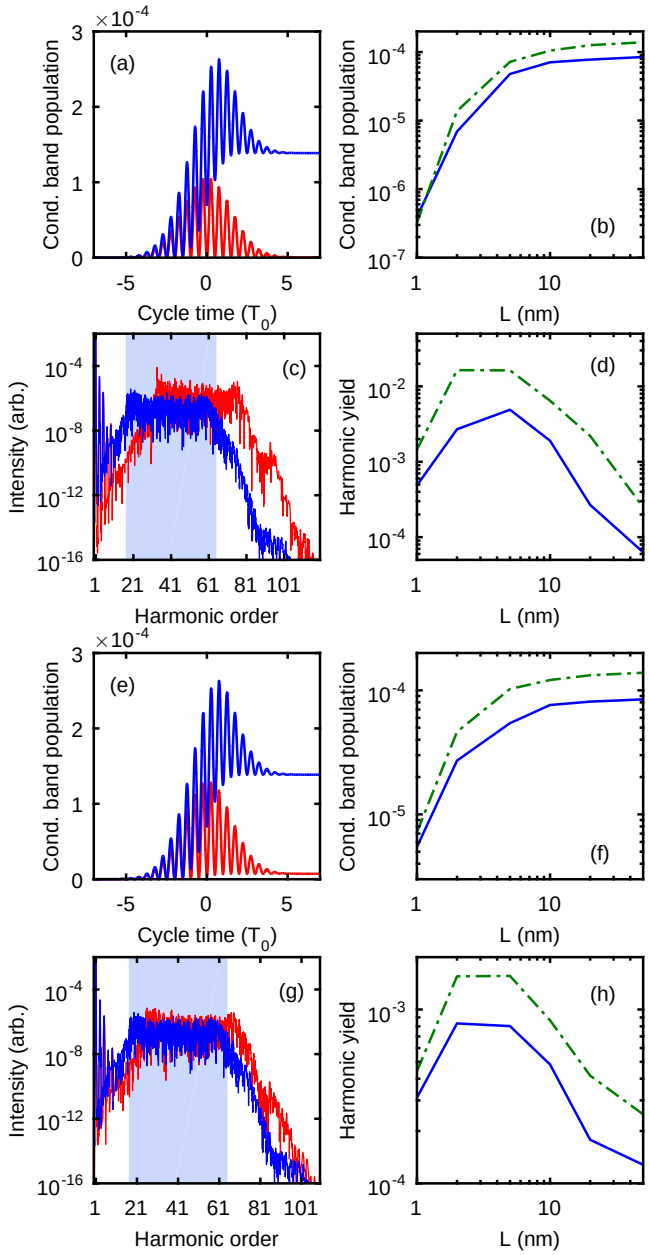

Figure 3.3: Panels (a)-(d) present results for our model system with confinement along both transverse directions. (a) Time-dependent conduction band population for $L = 50\,\text{nm}$ (blue) and $L = 1\,\text{nm}$ (red) with $\lambda_0 = 6.4\,\mu\text{m}$. (b) Conduction band population after the laser pulse has passed versus L for $\lambda_0 = 3.2\,\mu\text{m}$ (solid) and $\lambda_0 = 6.4\,\mu\text{m}$ (dash-dot). (c) Harmonic spectra for $L = 50\,\text{nm}$ (blue) and $L = 1\,\text{nm}$ (red). The shaded region shows the above band gap range $[E_L, E_L + \Delta_L]$ for the $L = 50\,\text{nm}$ system. The spectrum for $L = 1\,\text{nm}$ is shifted due to the increase in band gap and thus the region of integration is shifted accordingly. (d) Harmonic yield versus L for $\lambda_0 = 3.2\,\mu\text{m}$ (solid) and $\lambda_0 = 6.4\,\mu\text{m}$ (dash-dot). (e)-(h) Panels (a)-(d) repeated for confinement along a single transverse direction.

is reflected in Figs. 3.3(d) and 3.3(h) where the harmonic yield calculated from equation (3.6) is shown. In both cases there is an increase in harmonic yield from $L = 50\,\text{nm}$ to $L = 1\,\text{nm}$. However, the increase is greater when confinement is along both transverse directions. For $L < 3-4$ nm the increase in HHG is outweighed by the drop in ionization so that HHG efficiency declines with decreasing confinement width. The harmonic yield is higher for the longer wavelength mainly due to higher ionization. For the parameters used here, the wavelength dependence of the HHG process, after ionization, has already saturated at 3.2μm (see Fig. 3.5).

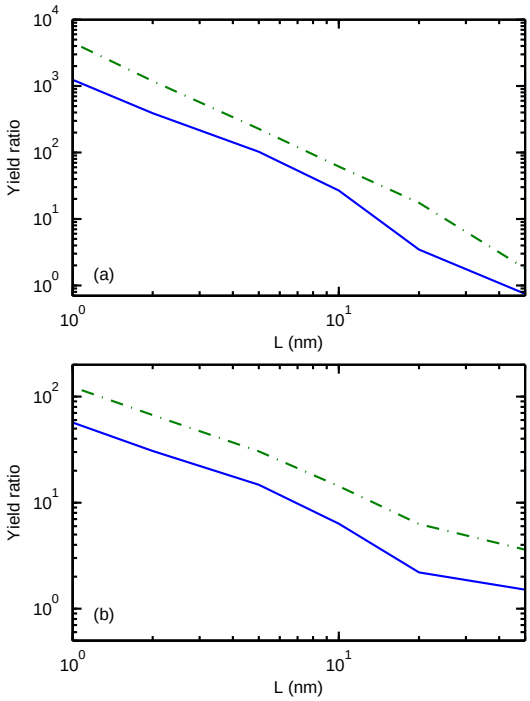

Figure 3.4: Yield ratio versus confinement width for $\lambda_0 = 3.2\,\mu$m (solid) and $\lambda_0 = 6.4\,\mu$m (dash-dot) for (a) the confinement along both transverse directions and (b) confinement along a single transverse direction.

The results presented in Fig. 3.3 show an increase in harmonic yield accompanied by a significant decrease in ionization. As such, it is useful to examine the yield ratio shown in Fig. 3.4. The yield ratio gives the harmonic yield per ionization event and constitutes a measure of how efficiently population promoted to the conduction band generates above band gap harmonic radiation. Figure 3.4(a) shows the yield ratio for the system with confinement along both transverse directions and Fig. 3.4(b) show the corresponding results when confinement is along a single transverse

direction. In both cases there is monotonic growth in yield ratio with decreasing confinement width. This implies that the efficiency, with which electrons promoted to the conduction band create harmonics, is increased as the system becomes more tightly confined. However, when confinement is along both transverse directions, the increase is significantly larger by couple orders of magnitude. Comparing the $L = 50\,\text{nm}$ to $L = 1\,\text{nm}$, there is an increase of nearly three orders of magnitude when both directions are confined as compared to about a single order of magnitude when confinement is along only one direction. As ionization is the first step in HHG, an increase in harmonic yield efficiency coupled with a decrease in ionization appears counter-intuitive; in what follows we will explain this observation.

3.4.2 The effect of confinement on diffusion and recollision

In Fig. 3.2 it was shown that quantum confinement causes an increase in the band gap and a reduction of the density of states along each direction of confinement. Both of these effects have an influence on ionization and high harmonic generation. By varying the width of the confinement, as is done in Figs. 3.3 and 3.4, these phenomena remain coupled. In order to gauge the importance of each of these contributions, it is necessary to separate them. This separation can be achieved by noting that the absolute limit of confinement occurs when there is only a single atom along each confined transverse direction. When confinement is along both transverse directions this limit is reached for an atomic chain. In the case of confinement along a single direction this limit is reached for an atomic monolayer. The single atom wire contains only a single doubly degenerate transverse state and therewith is an idealized one-dimensional system with the same band gap in which confined transverse coordinates are neglected. In a similar manner, the monolayer is identical to an idealized two-dimensional system in which the confined coordinate is ignored. Likewise, by neglecting the confined transverse coordinates of a 3D bulk material, the band gap of the resulting 1D and 2D mediums remain unaltered. However, the quantum confinement has now transformed from no confinement to maximum confinement. Thus, by comparing a 3D bulk medium with its corresponding 1D and 2D limits, the effect resulting solely from quantum confinement can be examined. Comparison of the 1D and 2D limits to the $L = 1$ nm confinement will allow for the effect resulting from the change in band gap to be quantified.

To compare the 3D bulk to its 1D and 2D limits, we compare the $L = 50\,\text{nm}$ systems with $q = 2$ and $q = 1$ with their respective 1D or 2D system where the confined transverse coordinates have been neglected. These results will be compared against equations (3.7) and (3.8) given in the previous chapter. Figure 3.5(a) displays the ratio of the final conduction band population calculated from equation (3.3) for the 1D system to the $L = 50\,\text{nm}$ system; Fig. 3.5(b) displays the corresponding result

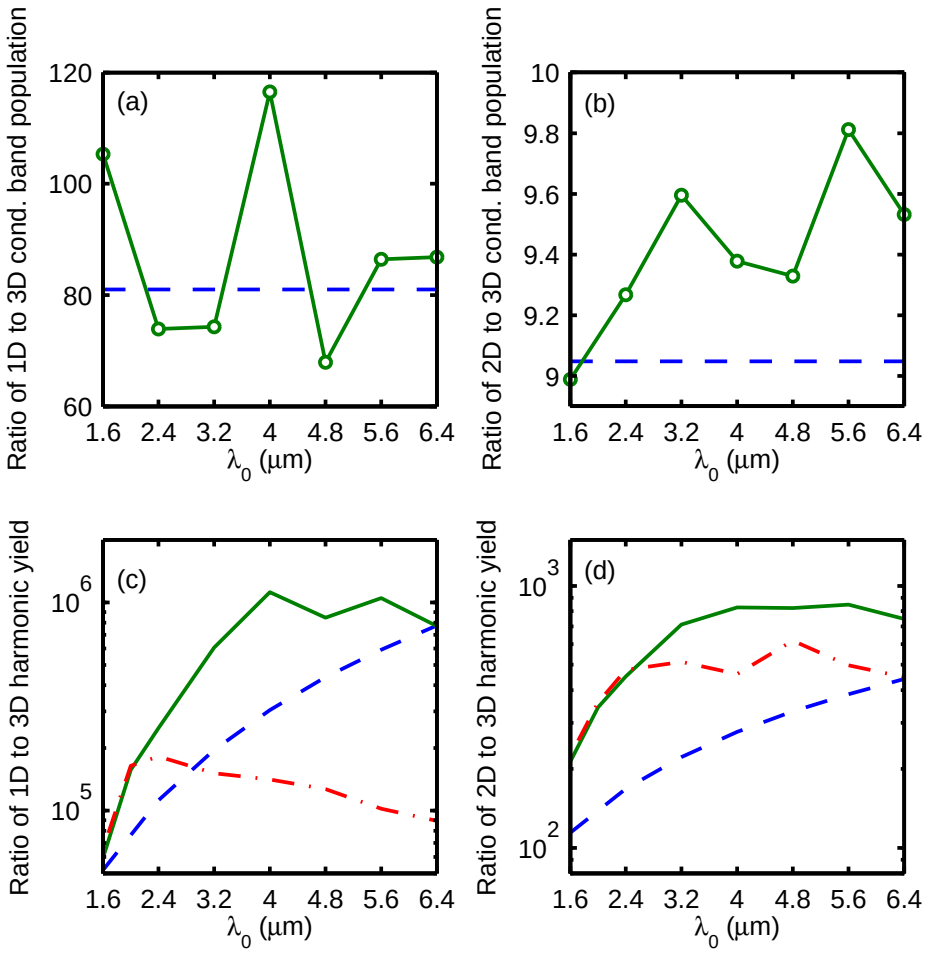

Figure 3.5: (a) Ratio of final conduction band population in the 1D system to the $L = 50\,\text{nm}$ system (circles with solid line) versus λ_0; the dashed line gives $(n_\perp^{2D})^{-1}$ predicted by equation (3.7). (b) Ratio of final conduction band population in the 2D system to the $L = 50\,\text{nm}$ system (circles with solid line) versus λ_0; the dashed line gives $(n_\perp^{1D})^{-1}$ predicted by equation (3.7). (c) Ratio of harmonic output from the 1D system to the $L = 50\,\text{nm}$ (solid) and the $L = 20\,\text{nm}$ (dash-dot) systems versus λ_0. The dashed line shows the prediction for $|j_\perp^{2D}|^{-2}$ from equation (3.8). (d) Ratio of harmonic output from the 2D system to the $L = 50\,\text{nm}$ (solid) and the $L = 20\,\text{nm}$ (dash-dot) systems versus λ_0. The dashed line shows the prediction for $|j_\perp^{1D}|^{-2}$ from equation (3.8).

for the 2D system. Both are compared to $(n_{\perp}^{qD})^{-1}$ from equation (3.7) (dashed line). Equation (3.7) is wavelength independent and the calculated results appear consistent with this. While the calculated results deviate from the constant value predicted by equation (3.7), given its simplicity and the complex nature of ionization in solids [56], these variations are not unreasonable. Furthermore, the results in Figs. 3.5(a) and 3.5(b) indicate that ionization is not strongly affected by the form of the wave packet at birth. Thus, the drop in ionization seen in Figs. 3.3(b) and 3.3(f) results mainly from the increase in the band gap.

Figure 3.5(c) shows the ratio of harmonic output calculated from equation (3.5) of the 1D system to the $L = 50\,\text{nm}$ (solid) and the $L = 20\,\text{nm}$ (dash-dot) systems with confinement along both transverse directions ($q = 2$); Fig. 3.5(d) shows the corresponding results for the ratio of harmonic output of the 2D system to the $L = 50\,\text{nm}$ (solid) and the $L = 20\,\text{nm}$ (dash-dot) with confinement along a single transverse direction ($q = 1$). In both cases, the numerical results are compared to $|j_{\perp}^{qD}|^{-2}$ predicted by equation (3.8) (dashed line). Equation (3.8) predicts that the ratio of 1D or 2D output to the 3D harmonic output will increase with wavelength. This rise results from reduced harmonic output of the 3D system due to quantum diffusion which decreases the electron-hole recombination cross section. For the $L = 50\,\text{nm}$ systems this ratio increases until about $4\,\mu\text{m}$ and then begins to saturate indicating a halt in spreading of the wave packet due to the confinement. Similar behaviour occurs for the $L = 20\,\text{nm}$ systems but saturation begins at a shorter wavelength. This is consistent with that expected from quantum diffusion. Longer wavelengths experience greater spreading of the transverse wave packet and will thus be affected more strongly by a narrower confinement. Further, this effect is much stronger for systems with confinement along both transverse directions. This occurs because less diffusion is permitted when both transverse coordinates are confined as opposed to a single coordinate, as in the 2D system. Finally, our analytical model reflects the trend correctly, but the λ_0^2 scaling in equation (3.8) understates the power scaling of the wavelength dependence. This indicates that the actual ionized transverse wave packet structure might be more complex than the approximate Gaussian distribution obtained in equations (3.7) and (3.8). Such a fact may also explain the unusual elliptic polarization dependence of HHG in solids observed by experiment [62].

3.5 Summary

In this chapter, we have presented the impacts of quantum confinement along one and two transverse directions on HHG. The effects of 1D and 2D confinement are qualitatively similar, they are substantially more pronounced in the nanowire. We have examined the fact that the quantum confinement causes a widening of the band gap and a reduction of the density of states. These two results have their direct impact on the ionization and harmonic yield. The increase of the band gap leads to a decrease of the final conduction band population. That results in a suppression of the ionization which presents an advantage since it leads to raising the damage threshold intensity of the material when the laser source is a few-cycle pulse. The few-cycle pulse is essential here to guarantee there are no other ionization channels except the optical field ionization. On the other hand, the reduction of the density of transverse states reduces quantum diffusion. This results in an increase of the recollision cross-section; therefore, an increase in the HHG efficiency.

Our results suggest that nano-engineering might present a way to surmount some of the restrictions placed on generating high order harmonics from semiconductor materials. Further, our findings offer a potential explanation for the increase in harmonic efficiency found in recent experiments, where bulk HHG was compared to atomically thin monolayers of crystalline MoS_2 [18].

Finally, our analysis is performed within the single electron approximation. In low dimensional materials, correlation effects can become significant; these effects are neglected in our investigation.

Future research can be concentrated on using stacked lower-dimensional systems to enhance the harmonic output. The use of these systems is a potential way to suppress the limitation that comes from absorption. In such systems, propagation occurs in the gaps between the material layers, where no reabsorption exists.

Chapter 4

Impurity Tomography

In 2004, Itatani et al. [25] proposed an experimental method to image the highest occupied electronic orbital of nitrogen. Their strategy is based on what has been introduced in Sec. (1.4). Other experiments demonstrated the reconstruction of orbitals for a more complex molecule such as carbon dioxide [24]. Here we translate this method from the gas to the solid state phase by using impurities. The problem of impurities in semiconductors has been mapped to the hydrogen-like atom by the effective mass theorem [63–65]; as compared to the hydrogen atom, electron mass and dielectric constant are different. Due to this similarity, we theoretically reconstruct the impurity wavefunction by the same method that has been introduced in imaging of molecular orbitals.

In this chapter, the three-step model for high harmonic generation from shallow donor impurity in solid is developed. Then, we use the model to investigate the tomographic reconstruction of the impurity ground state wavefunction from harmonic spectra. The impurity dipole moment is found to be the dominant factor in determining the magnitude of the harmonic signal as a function of harmonic order; ionization and propagation which have to be factored out in molecular tomography play a lesser role here. This indicates a substantial facilitation due to the potential for direct reconstruction of the impurity ground state from the harmonic spectrum.

4.1 HHG in doped semiconductors

In the following HHG from impurities driven by long wavelength, laser fields is investigated. Quantum equations of motion and a three-step model for this process are developed. Figure 4.1 depicts a schematic representation for HHG from shallow impurities in one dimension. In Fig. 4.1(a) we have the periodic potential of the

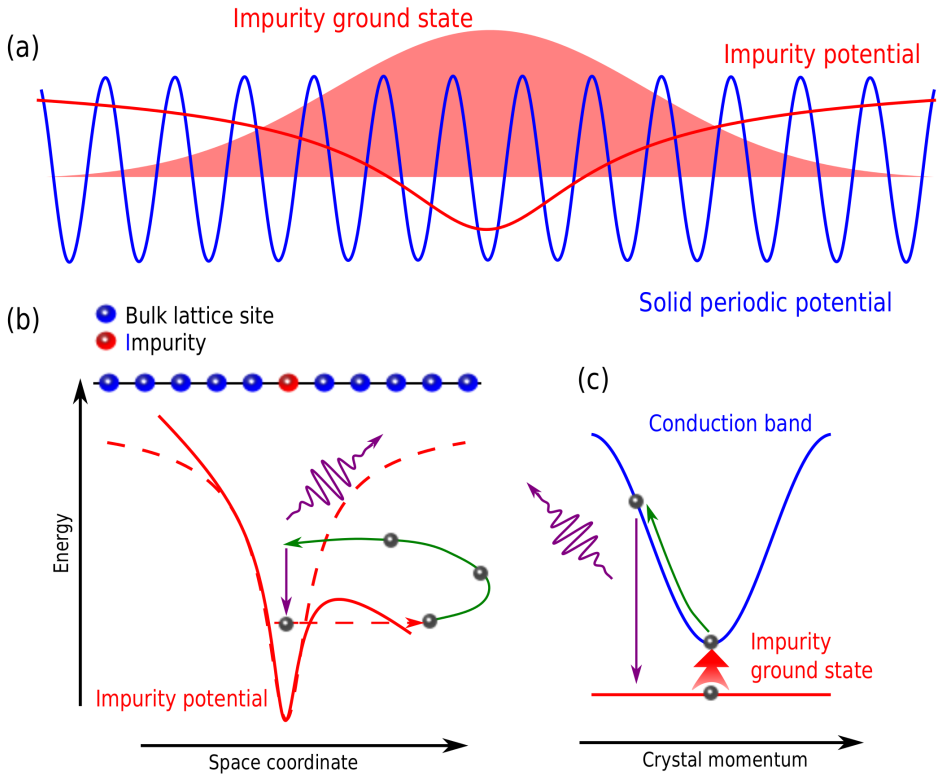

Figure 4.1: (a) Periodic potential of the unperturbed bulk solid (blue) plus the impurity potential (red); the shalloe impurity ground state that extends over many lattice cites is represented by the shaded curve. (b) Space representation of the three-step model for HHG from an impurity. (c) Reciprocal space representation of the three-step model for HHG from an impurity.

unperturbed solid (blue) plus a Coulomb potential from an impurity (red). The shaded curve represents the ground state of the shallow impurity; this ground state extends over many lattice cites. The semiclassical description of HHG is given by the three-step model. First, a free electron/hole is created in the conduction/valence band by tunnel ionization of a donor/acceptor impurity. Second, the electron/hole is accelerated by the laser field. In a third step a harmonic photon is emitted upon recollision and recombination with the parent impurity. The three-step model is shown in the real and reciprocal space in Figs. 4.1(b) and 4.1(c), respectively, for the system interacting with a strong laser field.

Besides differences in the continuum evolution due to the non-parabolic nature of bands, the process is found to be identical to HHG in gases. As a consequence, many processes can be adapted from the gas to the condensed matter phase. This opens a new research direction for atomic and molecular strong field processes.

4.1.1 Quantum mechanical model

Our one-body analysis builds on, and extends, the theoretical work by Adams [63] and by Luttinger and Kohn [64, 65]. We use the following model: an impurity with potential $U(\mathbf{x})$ is imbedded in a solid and is coupled to a laser field $\mathbf{F}(t)$ via the dipole coupling term $\mathbf{x} \cdot \mathbf{F}(t)$. The resulting time-dependent Schrödinger equation is given by

$$i\partial_t \Psi(\mathbf{x}, t) = \left(H_i - \mathbf{x} \cdot \mathbf{F}(t)\right) \Psi(\mathbf{x}, t), \tag{4.1}$$

where $H_i = H_0 + U(\mathbf{x})$ and $H_0 = \frac{1}{2}\mathbf{p}^2 + v(\mathrm{x})$ refers to the Hamiltonian of the solid without impurity with $v(\mathrm{x})$ being the periodic lattice potential. The eigenvalue equation of the field free Hamiltonian H_i is given by

$$H_i \phi(\mathbf{x}, t) = \varepsilon \phi(\mathbf{x}, t). \tag{4.2}$$

In the absence of the impurity the eigenfunctions $\Phi_{m,\mathbf{k}}$ fulfil $H_0 \Phi_{m,\mathbf{k}} = E_m(\mathbf{k}) \Phi_{m,\mathbf{k}}$ with m the band index and $E_m(\mathbf{k})$ the band eigenenergies. Further, the eigenfunctions are given by,

$$\Phi_{m,\mathbf{k}}(\mathbf{x}) = \frac{1}{\sqrt{V}} u_{m,\mathbf{k}}(\mathbf{x}) e^{i\mathbf{k}\cdot\mathbf{x}}, \tag{4.3}$$

where $u_{m,\mathbf{k}}$ is the Bloch function that is periodic with the lattice and V the volume of the solid. The unit cell is defined by basis vectors $\mathbf{a}_l$ ($l = 1, 2, 3$) and volume v; $\mathbf{R}_n = \sum_l n_l \mathbf{a}_l$ is a lattice vector that connects two identical sites in the lattice. The crystal momentum $\mathbf{k}$ extends over the first Brillouin zone (BZ) defined as the

Wigner-Seitz cell of the reciprocal lattice whose primitive vectors $\mathbf{b}_l$ are determined through $\mathbf{b}_l \cdot \mathbf{a}_j = 2\pi\delta_{lj}$; we denote the magnitude of the reciprocal lattice vector $\mathbf{b}_l$ as $b_l = |\mathbf{b}_l|$. The vectors of the reciprocal lattice are given by $\mathbf{K}_n = \sum_l n_l \mathbf{b}_l$. The eigenfunctions are orthonormalized according to,

$$\int_V \Phi^*_{m',\mathbf{k}'} \Phi_{m,\mathbf{k}} d\mathbf{x} = \delta_{mm'}\delta(\mathbf{k}-\mathbf{k}'). \tag{4.4}$$

By defining $V = N\upsilon$ with N the number of atomic unit cells, we obtain from the orthonormality relation $\int_v |u_{m,\mathbf{k}}|^2 d\mathbf{x} = \upsilon$.

Shallow donor (acceptor) impurities split into an electron (hole) and a positively (negatively) charged residual ion; the electron (hole) moves in the lowest conduction (highest valence) band and has bound states in the field of the residual ion with energies closely below (above) the bottom (top) of the conduction (valence) band. As a result, we drop the band index m and confine our treatment to a single band with eigenfunctions $\Phi_\mathbf{k}$ which fulfil $H_0\Phi_\mathbf{k} = E(\mathbf{k})\Phi_\mathbf{k}$ with $E(\mathbf{k})$ the band eigenenergies. Further, we consider a single impurity level (the impurity ground state) with eigenenergy ε_0 and eigenfunction ϕ_0; here Eq. (4.2) reads,

$$H_i\phi_0(\mathbf{x}) = \varepsilon_0\phi_0(\mathbf{x}). \tag{4.5}$$

As this is a first conceptual study we have limited ourselves to only the most fundamental process and confined our system to the ground state only. Additional complexity can be added to the model by including excited states of the impurity potential.

4.1.2 Derivation of the ground state for a shallow impurity

Equation (4.5) is solved by expanding the eigenstate ϕ_0 in terms of Bloch states,

$$\phi_0(\mathbf{x}) = \int_{\mathrm{BZ}} b_0(\mathbf{k})\Phi_\mathbf{k}(\mathbf{x}) d\mathbf{k}. \tag{4.6}$$

Inserting Eq. (4.6) into Eq. (4.5), multiplying the result by $\Phi^*_{\mathbf{k}'}(\mathbf{x})$ and integrating over the spatial coordinate yields,

$$\big(E(\mathbf{k}) - \varepsilon_0\big) b_0(\mathbf{k}) + \int_{BZ} \widetilde{U}(\mathbf{k},\mathbf{k}') b_0(\mathbf{k}') d\mathbf{k}' = 0 \tag{4.7}$$

with

$$\widetilde{U}(\mathbf{k},\mathbf{k}') = \int_V u^*_\mathbf{k}(\mathbf{x}) u_{\mathbf{k}'}(\mathbf{x}) U(\mathbf{x}) e^{i(\mathbf{k}'-\mathbf{k})\cdot\mathbf{x}} d\mathbf{x}, \tag{4.8}$$

where integration if performed over the crystal volume V. By noting that $u_{\mathbf{k}}$ is periodic with the unit cell, the Bloch functions in Eq. (4.8) can be expanded in a Fourier series,

$$u^*_{\mathbf{k}}(\mathbf{x})u_{\mathbf{k}'}(\mathbf{x}) = \frac{1}{\sqrt{\upsilon}}\sum_n M^{(n)}_{\mathbf{k},\mathbf{k}'}e^{-i\mathbf{K}_n\cdot\mathbf{x}} \tag{4.9}$$

with

$$M^{(n)}_{\mathbf{k},\mathbf{k}'} = \frac{1}{\sqrt{\upsilon}}\int_\upsilon u^*_{\mathbf{k}}(\mathbf{x})u_{\mathbf{k}'}(\mathbf{x})e^{i\mathbf{K}_n\cdot\mathbf{x}}d\mathbf{x}. \tag{4.10}$$

As a result, we obtain for the Coulomb matrix element

$$\widetilde{U}(\mathbf{k},\mathbf{k}') = \sum_n M^{(n)}_{\mathbf{k},\mathbf{k}'}\int_\upsilon U(\mathbf{x})e^{i(\mathbf{k}'-\mathbf{k}-\mathbf{K}_n)\cdot\mathbf{x}}d\mathbf{x} \tag{4.11}$$

By inserting the series expansion (4.9) into the orthonormality relation for the Bloch eigenfunction (4.4) we obtain the relation

$$\frac{1}{\sqrt{\upsilon}}\int_\upsilon M^{(0)}_{\mathbf{k},\mathbf{k}'}e^{i(\mathbf{k}-\mathbf{k}')\cdot\mathbf{x}}d\mathbf{x} = \delta(\mathbf{k}-\mathbf{k}'). \tag{4.12}$$

Note that expansion terms with $n \neq 0$ result in $\delta(\mathbf{k}-\mathbf{k}'-\mathbf{K}_n) = 0$, as $\mathbf{k},\mathbf{k}'$ are from the first BZ. Equation (4.12) yields

$$M^{(0)}_{\mathbf{k},\mathbf{k}'} = \frac{\sqrt{\upsilon}}{(2\pi)^3}. \tag{4.13}$$

For a soft potential whose main components correspond to wavelengths that are much smaller than the lattice spacing, $|\mathbf{k}-\mathbf{k}'| \ll b_l$ the lowest order Fourier term dominates and we obtain [63, 64]

$$\widetilde{U}(\mathbf{k}-\mathbf{k}') \approx \frac{\sqrt{\upsilon}}{(2\pi)^3}\int_\upsilon U(\mathbf{x})e^{i(\mathbf{k}'-\mathbf{k})\cdot\mathbf{x}}d\mathbf{x}. \tag{4.14}$$

where we have written $\widetilde{U}(\mathbf{k},\mathbf{k}')$ as $\widetilde{U}(\mathbf{k}-\mathbf{k}')$ to indicate that the argument in $\widetilde{U}$ of our approximate expression above depends only on the difference $\mathbf{k}-\mathbf{k}'$. Note that close to the Coulomb singularity this assumption is violated and higher order Fourier terms need to be included. Inserting Eq. (4.14) in Eq. (4.7) yields

$$\left(E(\mathbf{k})-\varepsilon_0\right)b_0(\mathbf{k}) + \int_{BZ}\widetilde{U}(\mathbf{k}-\mathbf{k}')b_0(\mathbf{k}')d\mathbf{k}' = 0. \tag{4.15}$$

For the sake of simplicity we focus here on direct bandgap materials; however the theory can be easily generalized to indirect semiconductors following the treatment in Refs. [64] and [65]. By invoking again the assumption that the potential is soft and couples only components $|\mathbf{k}-\mathbf{k}'| \ll b_l$, we can further simplify Eq. (4.15). The bound states extend over many unit cells corresponding to a narrow band of crystal momenta $b(\mathbf{k})$ centered about the Γ-point ($\mathbf{k}=0$). In real space this corresponds to a slowly varying modulation that is superimposed onto the Bloch eigenfunction,

$$B_0(\mathbf{x}) = \int_{BZ} b_0(\mathbf{k}) \exp(i\mathbf{k}\cdot\mathbf{x}) d\mathbf{k}. \tag{4.16}$$

As a result of the narrow width of $b(\mathbf{k})$ the conduction band can be Taylor expanded which yields

$$E(\mathbf{k}) \approx E_g + \sum_{i,j} \frac{1}{2}\beta_{ij} k_i k_j, \tag{4.17}$$

where $i,j = x,y,z$ and $\beta_{ij} = \partial_{k_i}\partial_{k_j} E$ is the inverse mass tensor that arises from the quadratic expansion of the band energy $E(\mathbf{k})$ about the Γ-point ($\mathbf{k}=0$), where the band energy $E(\mathbf{k}=0) = E_g$ is minimum.

Using Eqs. (4.16) and (4.17), in Eq. (4.15) we obtain an atomic-like Schrödinger equation for the impurity eigenstates

$$\left(\frac{1}{2}\sum_{i,j}\beta_{ij}\nabla_i\nabla_j - U(\mathbf{x}) + (\varepsilon_0 - E_g)\right) B_0(\mathbf{x}) = 0. \tag{4.18}$$

Diagonalization of Eq. (4.18) yields ground state wavefunction $B_0(\mathbf{x})$ and $b_0(\mathbf{k})$ in k-space. Its eigenenergy ε_0 determines the ionization potential as $\varepsilon_0 - E_g$. The complete impurity ground state is determined by inserting $b_0(\mathbf{k})$ into Eq. (4.6) which results in

$$\phi_0(\mathbf{x}) = \int_{\mathrm{BZ}} b_0(\mathbf{k})\Phi_{\mathbf{k}}(\mathbf{x}) d\mathbf{k} \approx \Phi_{\mathbf{k}=0}(\mathbf{x}) B_0(\mathbf{x}). \tag{4.19}$$

In the last step we have used $\Phi_{\mathbf{k}}(\mathbf{x}) \approx u_{\mathbf{k}=0}(\mathbf{x})\exp(i\mathbf{k}\cdot\mathbf{x})$, a result from $\mathbf{k}\cdot\mathbf{p}$ perturbation theory.

4.1.3 Solution of the time-dependent Schrödinger equation

Solution of the time-dependent Schrödinger equation (4.1) in the presence of a strong laser field is developed along the lines of strong field atomic physics [30, 37].

The wavefunction is split into a bound state part and a band contribution, by using the Ansatz

$$\Psi(\mathbf{x},t) = \phi_0(\mathbf{x}) + \int_{\mathrm{BZ}} a(\mathbf{k},t)\Phi_{\mathbf{k}}(\mathbf{x})d\mathbf{k}. \tag{4.20}$$

where the integral runs over the first BZ. We assume, in the spirit of the strong field approximation [30], that field induced ionization is weak enough so that the ground state population remains unaffected. This amounts to neglecting the dynamic Stark shift of the impurity ground state.

Inserting Eq. (4.20) into Eq. (4.1) and multiplying the resulting equation with the functional $\langle\Phi_{\mathbf{k}'}(\mathbf{x})|$ we obtain

$$\begin{aligned} i\frac{d}{dt}a(\mathbf{k},t) &= \left(E(\mathbf{k}) - \varepsilon_0 + i\mathbf{F}(t)\cdot\nabla_{\mathbf{k}}\right)a(\mathbf{k},t) \\ &+ \int_{BZ} U(\mathbf{k}-\mathbf{k}')a(\mathbf{k}',t)d\mathbf{k}' + i\mathbf{d}_0(\mathbf{k})\cdot\mathbf{F}(t), \end{aligned} \tag{4.21}$$

where the transition dipole moment between impurity ground state and conduction band is,

$$\mathbf{d}_0(\mathbf{k}) = \int_V \Phi^*_{\mathbf{k}'}(\mathbf{x})\mathbf{x}\phi_0(\mathbf{x})d\mathbf{x}. \tag{4.22}$$

Equation (4.21) is similar to the equation of atomic strong-field physics [30]. Around the Γ-point, where the effective mass approximation is valid, Eq. (4.21) becomes identical with the equation for atomic gases. We note, however, that in Eq. (4.21) the full band is used and not the effective mass approximated band in Eq. (4.17).

Here we have again employed the assumptions used for the derivation of the impurity potential matrix element (4.14) where a soft impurity potential is assumed for which large momentum scattering $|\mathbf{k}| > |\mathbf{b}_l|$ is negligible. In terms of dynamical processes, these assumptions amount to neglecting large angle scattering events of the order of or larger than the inverse lattice vectors, which occur when a slow electron comes close to the Coulomb singularity and undergoes scattering. Further the resulting intraband dipole matrix element is only well defined when written as [16]

$$\int_V \Phi^*_{\mathbf{k}'}(\mathbf{x})\mathbf{x}\Phi_{\mathbf{k}}(\mathbf{x})d\mathbf{x} = -i\boldsymbol{\nabla}_{\mathbf{k}} + \mathbf{d}_c(\mathbf{k}), \tag{4.23}$$

where

$$\mathbf{d}_c = -i\int_V \Phi_{\mathbf{k}'}(\mathbf{x})\boldsymbol{\nabla}_{\mathbf{k}}\Phi_{\mathbf{k}}(\mathbf{x})d\mathbf{x}. \tag{4.24}$$

We assume here inversion symmetric materials for which $\mathbf{d}_c = 0$. As long as impurity ground state and conduction band wavefunction vary slowly compared to the Bloch functions, the dipole moment between impurity ground state and conduction band is given by,

$$\mathbf{d}_0(\mathbf{k}) \approx \frac{1}{(2\pi)^3} \int_V \mathbf{x} B_0(\mathbf{x}) e^{-i\mathbf{k}\cdot\mathbf{x}} d\mathbf{x}. \tag{4.25}$$

Here we have applied again Eq. (4.13) to approximately eliminate the product of Bloch functions. We find that the dipole moment is proportional to the Fourier transform of the atom-like part of the impurity ground state, just as in the atomic strong field model. Finally, agreement with atomic strong field physics becomes complete, when the quadratic mass approximation is applied to Eq. (4.21) [30, 37].

In the strong field limit, the Coulomb potential in Eq. (4.21) is neglected. For impurities, additional justification comes from the fact that photoionization cross sections are well described by replacing the Coulomb with delta-function potentials [66]. Integration of the resulting Eq. (4.21) and inserting the result into the second term of Eq. (4.6) yields the time dependent evolution of the electron wavefunction in the conduction band as

$$a(\mathbf{k},t) = \int_{-\infty}^{t} dt' \mathbf{d}_0(\boldsymbol{\kappa}_{t'}) \cdot \mathbf{F}(t') e^{\int_{-\infty}^{t'} i\left(\varepsilon_0 - E(\boldsymbol{\kappa}_{t''}) + \frac{i}{T_2}\right) dt''} \tag{4.26}$$

where $\boldsymbol{\kappa}_{t'} = \mathbf{k} - \mathbf{A}(t) + \mathbf{A}(t')$ with vector potential determined by $\mathbf{F} = -d\mathbf{A}/dt$; further, a phenomenological dephasing time T_2 has been added.

Finally, high harmonic generation is determined by the current

$$\begin{aligned} \mathbf{j}(t) &= \frac{d}{dt} \int_V \mathbf{x} |\Psi(\mathbf{x},t)|^2 d\mathbf{x} \\ &= \frac{d}{dt} \int_{\mathrm{BZ}} a(\mathbf{k},t) \mathbf{d}_0^*(\mathbf{k}) d\mathbf{k} + \int_{\mathrm{BZ}} \Big(a^*(\mathbf{k}',t) a(\mathbf{k},t) \\ &\qquad \times \frac{1}{i} \int_V \Phi_{\mathbf{k}'}^*(\mathbf{x}) \boldsymbol{\nabla} \Phi_{\mathbf{k}}(\mathbf{x}) d\mathbf{x} \Big) d\mathbf{k}' d\mathbf{k} + \text{c.c.} \end{aligned} \tag{4.27}$$

The second term in Eq. (4.27), corresponding to the intraband current, comes as a result of changing the Schrödinger picture to the Heisenberg picture, using $d\mathbf{x}/dt = \mathbf{p}$ and then converting back to the Schrödinger picture. Further simplification can be made using the relation,

$$\frac{1}{i} \int_V \Phi_{\mathbf{k}'}^*(\mathbf{x}) \boldsymbol{\nabla} \Phi_{\mathbf{k}}(\mathbf{x}) d\mathbf{x} = \boldsymbol{\nabla}_{\mathbf{k}} E(\mathbf{k}) \delta(\mathbf{k} - \mathbf{k}') \tag{4.28}$$

with $\mathbf{v}(\mathbf{k}) = \boldsymbol{\nabla}_{\mathbf{k}} E(\mathbf{k})$ the band velocity. We then obtain

$$\mathbf{j}(t) = \mathbf{j}_i(t) + \mathbf{j}_{ra}(t), \tag{4.29}$$

where

$$\mathbf{j}_i(t) = \frac{d}{dt} \int_{\mathrm{BZ}} a(\mathbf{k}, t) \mathbf{d}_0^*(\mathbf{k}) d\mathbf{k} + \text{c.c.} \tag{4.30}$$

is the current due to the polarization buildup between band electron and impurity, and

$$\mathbf{j}_{ra}(t) = \int_{\mathrm{BZ}} |a(\mathbf{k}, t)|^2 \mathbf{v}(\mathbf{k}) d\mathbf{k} + \text{c.c.} \tag{4.31}$$

is the intraband current arising from the laser driven motion of the electron in the band; this contribution comes from the non-parabolicity of the band and is not present in HHG from atomic gases.

4.1.4 Semicalssical model for impurity high-harmonic generation

The high harmonic electric fields are determined by the polarization buildup between band and impurity ground state resulting in a current

$$\begin{aligned} \tilde{j}_i(\omega) = i\omega \int_{\mathrm{BZ}} d\mathbf{k}\, \mathbf{d}_0^*(\mathbf{k}) \int_{-\infty}^{\infty} dt e^{-i\omega t} \int_{-\infty}^{t} dt' \mathbf{d}_0(\boldsymbol{\kappa}_{t'}) \cdot \mathbf{F}(t') \\ \times e^{\left(iS(\mathbf{k},t',t) - \frac{1}{T_2}(t-t')\right) dt''} + \text{c.c.} \end{aligned} \tag{4.32}$$

where $S(\mathbf{k}, t', t) = \int_{t'}^{t} \big(\varepsilon_0 - E(\boldsymbol{\kappa}_{t''})\big) dt''$.

The three integrals in Eq. (4.32) can be solved analytically by the saddle point method [30]. The saddle point equations are determined by,

$$\nabla_{\mathbf{k}} S = \int_{t'}^{t} \mathbf{v}(\boldsymbol{\kappa}_{t''}) dt'' = \mathbf{x}(t) - \mathbf{x}(t') = 0 \tag{4.33a}$$

$$\frac{dS}{dt'} = E(\mathbf{k} - \mathbf{A}(t) + \mathbf{A}(t')) - \varepsilon_0 = 0 \tag{4.33b}$$

$$\frac{dS}{dt} = E(\mathbf{k}) - \varepsilon_0 = \omega. \tag{4.33c}$$

In Eq. (4.33a), the band velocity is given by $\mathbf{v}(\mathbf{k}) = \boldsymbol{\nabla}_{\mathbf{k}} E$. This equation states that HHG can take place only when the electron, born at time t' into the band, returns to the parent impurity at t. Equation (4.33b) states that electrons are born with zero momentum at time t', $\mathbf{k} = \mathbf{A}(t = t') - \mathbf{A}(t') = 0$. At the time of

recombination t the electron crystal momentum is given by $\mathbf{k}(t',t) = \mathbf{A}(t) - \mathbf{A}(t')$. The finite impurity gap energy results in a complex birth time, which is responsible for tunnel ionization. Finally, Eq. (4.33c) represents conservation of energy — the electron recombines to the ground state and emits a photon ω with energy equal $E(\mathbf{k}(\mathbf{t}',\mathbf{t})) - \varepsilon_0$. Again, at moderate laser intensities, for which the effective mass approximation applies, the saddle point equations for atom and impurity become identical.

After saddle point integration we obtain for the harmonic intensity

$$\left|\tilde{j}_i(\omega)\right|^2 = \left|\sum_{t'} \sqrt{\mathrm{w}(t')}\mathbf{d}_0^*(\mathbf{k})\alpha(t',t)e^{\int_{t'}^{t}\left(i\mathcal{S}-\frac{1}{T_2}\right)dt''}\right|^2, \tag{4.34}$$

where $\mathcal{S} = \varepsilon_0 + \omega - E\big(\mathbf{k}(t'',t)\big)$, $\mathrm{w}(t')$ is the ionization rate and $t'(t(\omega))$ and $t(\omega)$ are birth and recombination times resulting in the generation of a harmonic with frequency ω. For an isotropic lattice the ionization rate is determined by the ADK tunnel ionization rate of atoms [67] with the electron mass replaced by the effective mass. Further, the dipole moment represents the recombination amplitude; the remaining term α in the pre-exponential is the propagation amplitude accounting for quantum diffusion and dephasing; this depends on the band specifics. For isotropic materials in the effective mass m approximation $\alpha \propto m\exp(-(t-t')/T_2)(t-t')^{-3/2}$. The main difference between HHG from impurities and atoms arises from the finite, non-parabolic, anisotropic nature of bands.

4.2 Numerical details

For the analysis of HHG tomography of impurities we use a 1D model system for a direct band gap semiconductor. The periodic lattice potential is composed of lattice cells of width $a = 9.45\,\text{a.u.} = 5\,\text{Å}$ and well depth $v_0 = 0.55\,\text{a.u.} = 15\,\text{eV}$. The lattice cells are separated by a mollifier function, see Section.(3.3.1); the lattice cell centered at $x = 0$ is given by,

$$v(x) = \begin{cases} v_0 e^{-\frac{(x+a/2)^2}{\sigma^2-(x+a/2)^2}} - v_0 & \text{for } -\frac{a}{2} \le x < -\frac{a}{2}+\sigma \\ v_0 e^{-\frac{(x-a/2)^2}{\sigma^2-(x-a/2)^2}} - v_0 & \text{for } \frac{a}{2}-\sigma < x \le \frac{a}{2} \\ -v_0 & \text{otherwise} \end{cases} \tag{4.35}$$

where σ represents the extension of the mollifier. Each cell is represented on a space grid of 40 points giving a grid spacing of $\Delta x = 0.236$. We use 400 cells to the left and right of the central cell for a total of 801 cells. The Coulomb potential is

centered over the central cell and is given by,

$$U(x) = \frac{-1}{\epsilon\sqrt{x^2 + s^2}}, \tag{4.36}$$

where s is the softening parameter and ϵ is the dielectric constant. For our model we use $s = 25$ a.u. and $\epsilon = 5$ a.u.

The Hamiltonian is diagonalized using periodic boundary conditions in both the presence and absence of the Coulomb potential. In the absence of the Coulomb potential we obtain the Bloch functions $\Phi_k(x)$; the energy gap between the highest valence band and lowest conduction band at the $\Gamma-$point is approximately 4 eV. When the Coulomb potential is present we obtain the impurity ground state; for this system the impurity ground state lies at an energy of 106.4 meV below the $\Gamma-$point of the conduction band. Figure 4.2(a) shows the calculated conduction band versus the crystal momentum k. In Fig. 4.2(b) the dipole moment calculated from Eq. (4.25) is shown.

The system is irradiated by a laser field with vector potential $A(t) = -(F_0/\omega_0)$ $f(t)\sin(\omega_0 t)$ with peak field strength F_0 and center frequency ω_0. The peak field strength is $F_0 = 1 \times 10^{-4}$a.u. which corresponds to a peak intensity of $I_0 = 3.5\times10^8$ W/cm^2 in the material. For the center frequency we use $\omega_0 = 9.1\times10^{-4}$ a.u.; this corresponds to a wavelength of $\lambda_0 = 50\,\mu$m. The pulse has a Gaussian envelope $f(t)$ with a FWHM of $12T_0$; here $T_0 = 2\pi/\omega_0 = 166$ fs. The time dynamics of the system are determined from Eq. (4.26) with $T_2 = 50$ fs. The dephasing time T_2 is chosen such that it is similar to dephasing times in semiconductors [68–70].

The parameters of our laser pulse and model system result in a result in a minimum $n = 5$ photon transition from impurity ground state to the conduction band using a pulse with an intensity of the order of 10^8 W/cm^2. For comparison ZnO has a $\Gamma-$point energy of 3.3 eV between the highest valence and lowest conduction band; doping with impurities such as H, Ga, Al and In leads to impurity donor states in the range $46 - 73$ meV [71]. For a similar $n = 5$ photon transition, such a system would require a laser pulse with central wavelength $\sim 100\,\mu$m with intensity ~ 100 MW/cm^2 which is achievable [72]. By contrast ZnSe has a bandgap of 2.8 eV with a donor level 1.2 eV below the bottom of the conduction band when doped with V [73]. Thus, the parameters chosen here give a reasonable approximation to a semiconductor with shallow donor impurity levels.

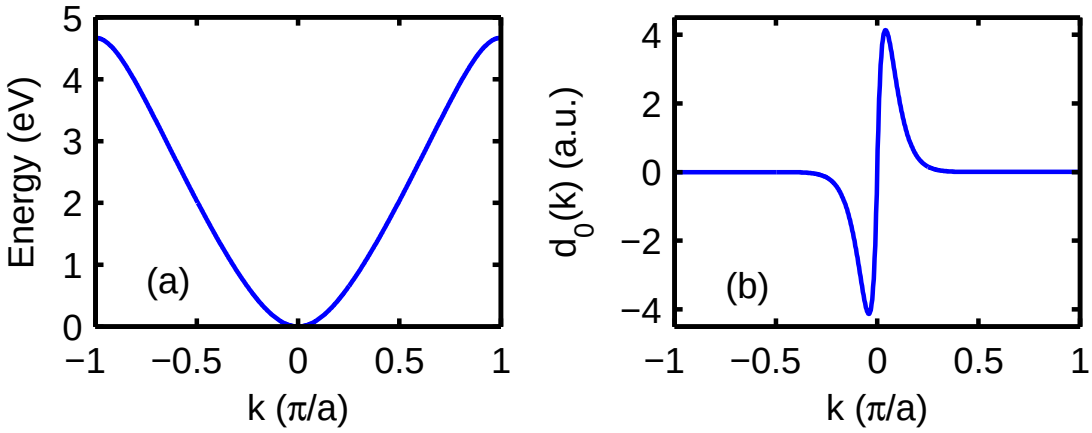

Figure 4.2: (a) Structure of the conduction band obtained from diagonalization of the Hamiltonian. (b) Dipole moment calculated using Eq. (4.22).

4.3 Tomographic reconstruction of the impurity state

Figure 4.3(a) shows the generated harmonics versus birth (red) and recombination (blue) times from the semiclassical trajectories obtained from numerical solution of Eqs. (4.33). There are two sets of solutions per optical cycle, a short and a long trajectory. The long trajectory contributions are indicated by the shaded regions in Fig. 4.3.

Figures 4.3(b)-(d) examine the behavior of each of the pre-exponential terms in Eq. (4.34). Figures 4.3(b) and 4.3(c) present the ionization rate and propagation term, respectively. For ionization we have used the dominant atomic tunneling exponent [30, 37].

Figure 4.3(d) shows $|d_0(\omega)|^2$ obtained from the diagonalization of the Hamiltonian (blue line), where k has been replaced with ω by virtue of relation (4.33c). We find that $|d_0(\omega)|^2$ decreases by about six orders of magnitude with increasing harmonic order. The rapid drop comes from the fact that the ground state extends over many unit cells and therewith populates only a small fraction of the BZ. In Fig. 4.3(d) we also plot the product of all three terms, where long and short trajectories are indicated by red dots and green squares, respectively. The short trajectories are dominant and a comparison with $|d_0(\omega)|^2$ shows that the dipole moment determines the form of the harmonic spectrum over most of its range; this is confirmed in Fig. 4.4.

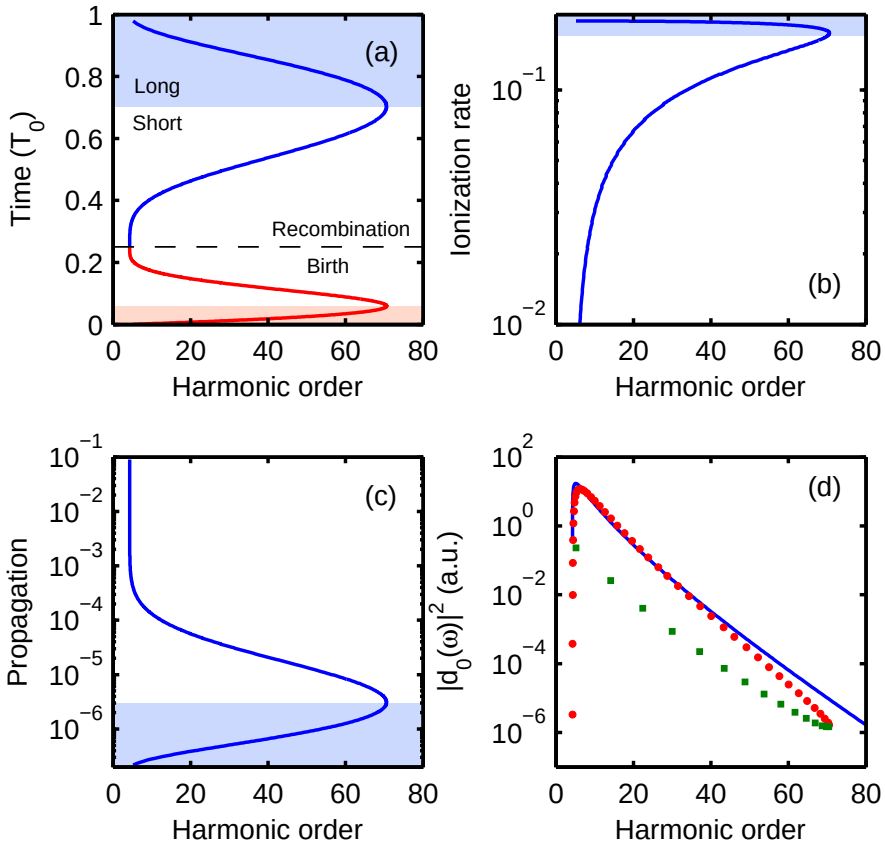

Figure 4.3: (a) Birth time t' (red) and return times t (blue) from the semiclassical trajectories versus harmonic order. (b) Ionization rate w $\propto \exp\big(-\frac{2}{3}\sqrt{m}(2(E_g-\varepsilon_0))^{3/2}/F(t')\big)$ versus harmonic order. (c) Propagation effects $\alpha^2 \propto \exp\big(-2(t-t')/T_2\big)/(t-t')$ versus harmonic order. (d) Magnitude squared of the dipole moment as a function of harmonic order (blue); the product of the three pre-exponential terms in Eq. (4.34) represented by blue lines in (b)-(d) is plotted for the short (red dots) and long (green squares) trajectory branches; the magnitude is adapted to match the dipole moment. In (a) - (c) the shaded regions indicate the contributions from long trajectories.

In Fig. 4.4 the harmonic intensity $|\tilde{j}|^2$ (blue) is plotted, including both the impurity and intraband contributions. We note that the harmonics above the impurity ionization potential are dominated by the impurity term (see Appendix B). The strength of the above impurity gap harmonics drops rapidly until around the cut-off near the 71^{st} harmonic. This behavior is consistent with the decrease of $|d_0(\omega)|^2$ (dashed) indicating that, of the three pre-exponential terms in Eq. (4.34), the dipole has the strongest influence on the shape of the harmonic spectrum. Consequently, using relation (4.33c) to connect harmonic order and k, we can reconstruct $d_0(k)$ from the magnitude of the harmonic spectrum. This is feasible, as the atom-like dipole moment is purely real/imaginary. For a complex dipole moment the phase of the harmonics must be considered, as in reference [74].

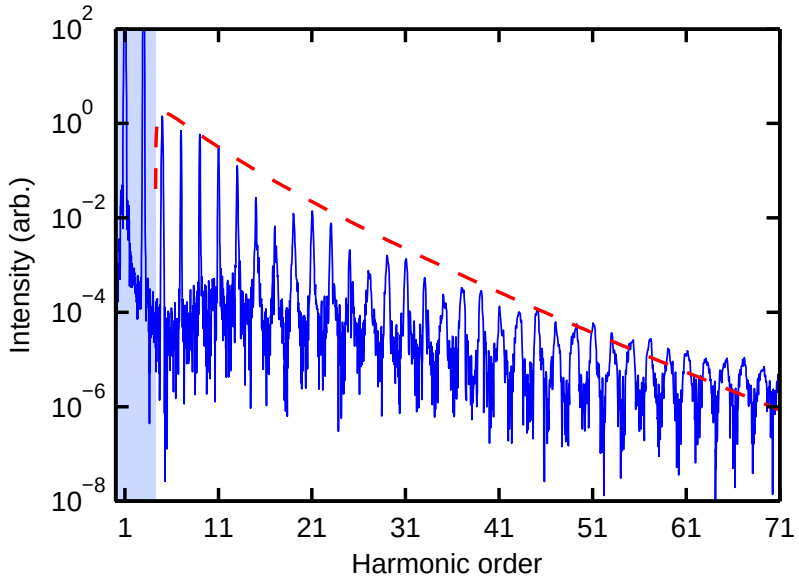

Figure 4.4: Scaling comparison of the harmonic spectrum (blue) to the dipole (red, dashed); the dipole has been shifted down in order to compare with the spectrum. The harmonics in the shaded region are those whose energy is below $E_g - \varepsilon_0$.

To reconstruct the impurity ground state we take the inverse Fourier transform of $d_0(k)$ and divide it by x to obtain $B_0(x)$. In a 3D experiment one would rotate the crystal and reconstruct the total wavefunction from 1D snapshots. Figure 4.5 shows the results of the tomographic reconstruction. The reconstructed wavefunction (red) matches the impurity ground state well throughout the central region but deviates from the true wavefunction at the tails. This agrees with the fact that the difference between harmonic intensity and dipole scaling in Fig. 4.4 is biggest for small crystal momenta corresponding to slow wavefunction variations in real space. Further the

small oscillations in the harmonic spectrum in Fig. 4.4 do not appear to cause a substantial error in the reconstruction; they result from interference between harmonics generated in positive and negative half-cycles as a consequence of the phase term in Eq. (4.34).

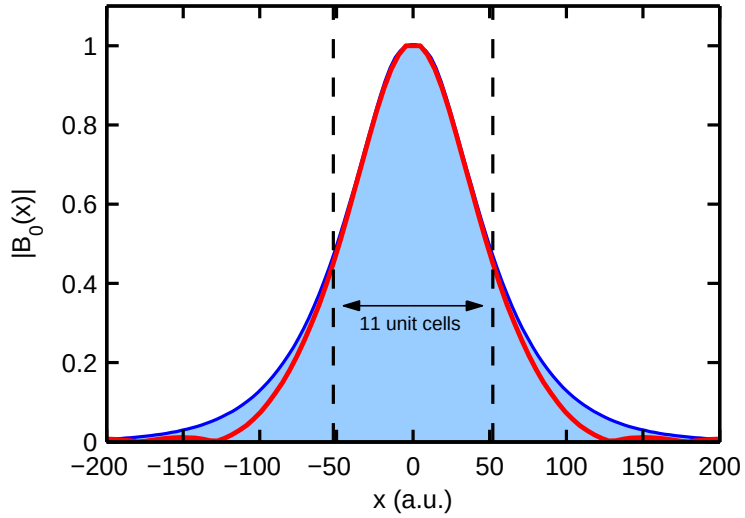

Figure 4.5: Comparison between the impurity ground state (blue, shaded) and the reconstructed ground state (red). The region between the vertical dashed lines represents 11 unit cells.

4.4 Dimensionality considerations for tomographic reconstruction

In our semiclassical model the ionization rate $\mathrm{w}(t')$ and the propagation term that accounts for quantum spreading and dephasing $\alpha(t', t)$, are given by,

$$\mathrm{w}(t') \propto e^{-\frac{2}{3}\sqrt{m}(2E_0)^{3/2}/F(t')} \tag{4.37a}$$

$$\alpha(t', t)^2 \propto \frac{e^{-2(t-t')/T_2}}{(t-t')^D} \tag{4.37b}$$

where $E_0 = E_g - \varepsilon_0$ is the impurity ionization potential, $D \in \{1, 2, 3\}$ is the dimension and t' and t are the birth and recombination times, respectively. The effective mass along the direction longitudinal to the laser polarization is given by m. In Eq. (4.37b) the term $(t-t')^{-D}$ accounts for the quantum spreading and the term $e^{-2(t-t')/T_2}$ accounts for the effect of dephasing. Both terms have the strongest effect on the long trajectories as $(t-t')$ will be greatest for this trajectory branch.

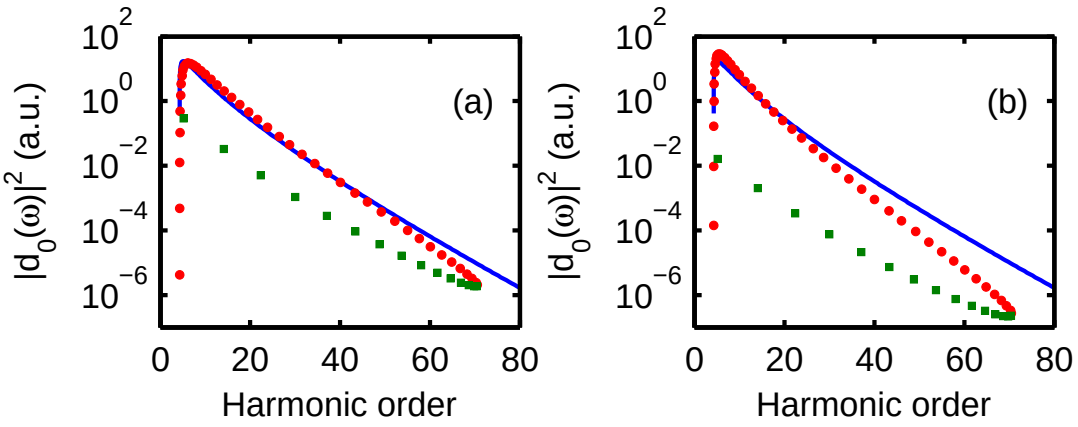

Figure 4.6: Magnitude squared of the dipole moment as a function of harmonic order (blue); the product of the three pre-exponential terms in Eq. (2.51) of the main manuscript is plotted for the short (red dots) and long (green squares) trajectory branches for (a) the one-dimensional system and (b) a three-dimensional system. The magnitude of the semiclassical curves is adapted to match the dipole moment.

The exponential scaling of the ionization rate only depends on the longitudinal components of the system along the direction of laser polarization; the transverse components only appear in the pre-exponential factor. As such, the dimensionality of the system is not expected to have a significant effect on the form of the ionization rate. Contrastingly, the quantum diffusion contribution $(t-t')^{-D}$ to the propagation term in Eq. (4.37b) will exhibit greater spreading for a three-dimensional system as opposed to a one-dimensional system.

Figure 4.6 shows the effect the dimension will have on the product $\mathrm{w}(t')\ |d_0(k(t', t))|^2\alpha(t', t)^2$ in Eq. (4.34). Figure 4.6(a) shows this product for the one-dimensional system; this is a reproduction of Fig. 4.3(d). Figure 4.6(b) shows the product with $D = 3$. The three-dimensional plot displays two main difference from the one-dimensional case. First, the separation between the long and short trajectory branches is greater in three dimensions than in one dimension. This occurs because spreading can occur in all three directions in the three-dimensional case. Secondly, because the spreading term is more pronounced in three-dimensions, the semiclassical curve deviates more from the behaviour of the dipole. This suggests that, for three-dimensional systems, it may be necessary to account for quantum diffusion before reconstructing the wavefunction. Accounting for quantum diffusion should be achievable in a straightforward manner using Eq. (4.34). For each birth and recombination time pair, $\alpha(t', t)$ can be calculated. This (t', t) pair corresponds to a particular harmonic and thus, we have the mapping $\alpha(t', t) \to \alpha(\omega)$. The $\alpha(\omega)$ term can then be factored out of the harmonic spectrum, removing the effect of

quantum diffusion for harmonic with frequency ω.

4.5 Summary

Because of the similarity between an atomic system and a doped semiconductor with donor impurities, one can apply the physics of HHG tomography in atoms and molecules on the doped semiconductor to image the wave function of the impurity ground state.

We calculate the harmonic spectrum by factorizing its three contributions: ionization, propagation, and recombination dipole. Our 1D harmonic spectrum calculation depicts that the dipole moment has the most significant influence on the harmonic spectrum shape. Prominently, there is a small dissimilarity between the spectrum and the dipole moment that gets greater for small crystal momenta.

Following the same procedure as in the atomic strong field, the inverse of Fourier transform of the dipole moment between the impurity state and conduction band divided by x gives the image of the impurity wave function. The reconstructed wave function matches the impurity wave function at the center, but it deviates at the ends. This deviation harmonizes with the difference between the spectrum and the dipole scaling. For 3D calculation, one must consider quantum diffusion before reconstructing the wavefunction. That is because the spreading occurs in three directions, unlike our calculations where it plays an insignificant role.

A more sophisticated reconstruction scheme could also remove the effects stemming from ionization. As a result of the complexity in calculating ionization rates in solids [56, 75–78], the ionization rate could be measured by transient absorption spectroscopy [57] and then factored out of the harmonic spectrum in a similar manner to that described for removing the effects of quantum diffusion. Furthermore, the dipole moment extracted from Eq. (4.34) or from numerical analysis can be improved on by using optimization techniques, similar to the one used recently for all optical band gap measurements [79]. Finally, for non-centrosymmetric materials the phase of the dipole is also important [80], facilitating the need for the phase of the harmonics to be measured for proper reconstruction.

Conclusions

High harmonic generation from low-dimension and doped semiconductors has been investigated in this dissertation. The effect that quantum confinement along one or two transverse directions has on high harmonic generation in semiconductor materials has been theoretically investigated. By reducing the density of states along the confined transverse direction, quantum spreading is reduced and the probability of recollision is increased. Further, the band gap is widened resulting in a higher damage threshold of the material. While the population transferred to the conduction band decreases monotonically with increasing confinement, the efficiency with which this population creates above band gap harmonics is increased. Further, this effect is enhanced when confinement is along both transverse directions as compared to a single direction. These results suggest that nanoengineering in semiconductor materials may provide an avenue for systematically increasing harmonic efficiency is solids exposed to intense laser fields.

A simple picture of the main physical mechanisms has been developed at the neglect of correlation effects. For low dimensional, tightly confined systems, correlation effects can become strong. This will restrict the amount by which the minimum band gap is increased as the confinement width is lowered. Further, in confined systems, electrons and holes experience stronger Coulomb interaction [81, 82] leading to an increased recollision probability and, by extension, further enhancement of HHG [18].

We conclude by noting that our investigation is microscopic in nature, meaning that propagation effects have been neglected. A primary limitation to bulk HHG comes from reabsorption of the generated harmonic radiation. Using confined systems such as nanowires or slabs made up of a few atomic monolayers can potentially mitigate this limitation, as the effective density of arrays of these confined systems is considerably lower than the bulk density. Due to the resulting longer interaction lengths phase mismatch between fundamental and harmonic beam might become relevant. Exploring these effects will be subject to future research.

As an application of HHG in doped semiconductors, we have presented the microscopic theoretical underpinning for exploring strong field physics in impurities. Our work makes a first step toward adapting technology developed for atomic and molecular gases to solid state impurities. In contrast to gases, absorption will limit the material depth from which photons and electrons can be detected; as a result, propagation effects are expected to be less significant. Whether experimental tomographic reconstruction is as straightforward as found here remains to be seen. How dominant the dipole moment is in determining harmonic spectra will depend on various factors, such as dephasing time, material dimension and parameters. Further, it has been demonstrated that for HHG to be viable, coherent buildup due to phase matching and field propagation effects should be considered [83]. To study these effects it would be necessary to couple the present theory to Maxwell's equations. This is beyond the scope of the current work and will be considered in a followup work.

Our results create a link between strong field physics and solotronics — solitary impurity electronics; for a review see Ref. [84]. Solitary impurities are important building blocks for quantum technology — as qubits for quantum computing and as single photon and non-classical photon sources for quantum sensing and communication. Further, with increasing miniaturization, the device characteristics of metal–oxide–semiconductor field-effect transistor (MOSFET) is strongly influenced by scattering off single impurities. All of the above applications require detailed knowledge about the wavefunction of impurity and environment. Currently, the most powerful method to image the wavefunction of single impurities is scanning tunneling microscopy close to suitably cleaved surfaces. Our results reveal that strong field methods can offer complementary capacities. Among other things they provide an all-optical way to measure dipole moment and wavefunctions of impurity ensembles independent of surfaces; single impurity imaging will be challenging due to the low quantum yield of HHG. Beyond that, they open the path to spatio-temporal imaging of wavefunction dynamics in impurities, impurity molecules and arrays [84] via optical pump probe experiments.

Finally, it needs to be discussed that our theoretical approach has been developed for shallow impurities. Deep impurities are more complex, as their wavefunction changes substantially over a unit cell. This results in a strong mixing between impurity and surrounding lattice wavefunction components. The resulting many-body effects, such as coupling to quasi-particles, need to be addressed with more sophisticated theoretical approaches [84]. They will dominantly enter in the dipole moment and therewith in recombination; ionization will be influenced to a lesser

extent, as the dipole moment enters in the pre-exponent. Propagation will only be altered close to the impurity, where the impurity potential yields higher-order corrections to the strong field approximation. As a result, our simple approach will present a reasonable starting point to develop strong field impurity physics in this more complex limit.

Appendix A

Derivation of transverse population and current

In this appendix we present a derivation of equations (3.7) and (3.8) for the transverse population $n_{\perp}^{qD}$ and current $|j_{\perp}^{qD}|^2$. From equation (3.3) we begin by writing the ionization rate $\dot{n}_c(t)$ as,

$$\dot{n}_c(t) = \mathcal{N}\int_{\overline{\mathrm{BZ}}} d^3K \Omega^*(\mathbf{K},t)\int_{-\infty}^{t} dt' \Omega(\mathbf{K},t') e^{iS(\mathbf{K},t,t')} + \text{c.c.}, \tag{A.1}$$

where the action integral is,

$$S(\mathbf{K},t,t') = \int_{t'}^{t} \varepsilon\Big(\mathbf{K}+\mathbf{A}(t'')\Big)dt''. \tag{A.2}$$

The vector potential is written as,

$$\mathbf{A}(t) = \hat{z}A(t) = \hat{z}(F_0/\omega_0)\cos(\omega_0 t) \tag{A.3}$$

and the band gap as,

$$\varepsilon(\mathbf{k}_\perp, K_z + A(t)) = \overline{E}_g(\mathbf{k}_\perp) + \Delta \sin^2\left(\frac{a_z}{2}\big(K_z + A(t)\big)\right) \tag{A.4}$$

where $\overline{E}_g(\mathbf{k}_\perp) = E_g + \varepsilon_\perp(\mathbf{k}_\perp)$ with E_g the minimum band gap and $\varepsilon_\perp$ the band gap transverse to the field polarization; the second term on the right hand side of equation (A.4) is the longitudinal band gap $\varepsilon_\parallel(k_z) = (\Delta/2)\big(1-\cos(k_z a_z)\big)$ in the nearest neighbour approximation. Further, the interband current can be written as [16],

$$\mathbf{j}(t) = -i\mathcal{N}\frac{d}{dt}\int_{\overline{BZ}} d^3K \mathbf{d}^*\big(\mathbf{K}+\mathbf{A}(t)\big)\int_{-\infty}^{t} dt' \Omega(\mathbf{K},t') e^{iS(\mathbf{K},t,t')} + \text{c.c.} \tag{A.5}$$

Both equations (A.1) and (A.5) contain the same term in the exponential and thus the saddle point integration for both will proceed similarly until the final steps.

Following an approach similar to that of Keldysh/Lewenstein [30, 37], we write the saddle point conditions $\partial_{t'}S = 0$ and $\partial_{K_z}S = 0$ from equation (A.1); these are given as,

$$\overline{E}_g(\mathbf{k}_\perp) + \Delta \sin^2\left(\frac{a_z}{2}\big(K_z + A(t')\big)\right) = 0 \tag{A.6}$$

$$\int_{t'}^{t} v_z\Big(K_z + A(t'')\Big)dt'' = 0 \tag{A.7}$$

where $v_z = \partial_{K_z}\varepsilon$. From equation (A.6) we have,

$$\sin\left(\frac{a_z}{2}\big(K_z + A(t')\big)\right) = \pm i\sqrt{\frac{\overline{E}_g}{\Delta}} \tag{A.8}$$

where for ease of notation we have dropped the $\mathbf{k}_\perp$ argument from $\overline{E}_g$. This allows us to write,

$$K_z + A(t') = \pm i\frac{2}{a_z}\sinh^{-1}\left(\sqrt{\overline{E}_g/\Delta}\right) = \pm i\alpha. \tag{A.9}$$

Inserting the complex saddle point $\tau + i\delta$ into equation (A.9) along the definition of $A(t)$ yields,

$$K_z + \frac{F_0}{\omega_0}\cos\Big(\omega_0(\tau + i\delta)\Big) = \pm i\alpha. \tag{A.10}$$

Using the trigonometric identity $\cos(x+y) = \cos(x)\cos(y) - \sin(x)\sin(y)$ and equating the real and imaginary parts, equation (A.10) gives,

$$K_z + A(\tau)\cosh(\omega_0\delta) = 0 \tag{A.11}$$

$$\frac{F(\tau)}{\omega_0}\sinh(\omega_0\delta) = \pm g(\mathbf{k}_\perp). \tag{A.12}$$

Here, $g(\mathbf{k}_\perp)$ is given by,

$$g(\mathbf{k}_\perp) = \frac{\alpha\omega_0}{F(\tau)} \approx \frac{\omega_0}{F(\tau)}\sqrt{2m_z\overline{E}_g} \tag{A.13}$$

where $m_z^{-1} = \partial^2_{K_z}\varepsilon|_{K_z=0} = \Delta a_z^2/2$ is the effective electron mass. At $\mathbf{k}_\perp = 0$, the expression in equation (A.13) becomes the well known Keldysh parameter γ [37]. For the parameters used in the main text, $\gamma < 1$ which means that tunneling is the dominant ionization mechanism.

For $\gamma < 1$, we can write $\cosh(\omega_0\delta) \approx 1$ in equation (A.11) and $\sinh(\omega_0\delta) \approx \omega_0\delta$ from equation (A.12). With that, our saddle point in the tunnelling limit is characterized by,

$$K_z + A(\tau) = 0 \tag{A.14}$$

$$\delta \pm \sqrt{\frac{2m_z\overline{E}_g}{F^2(\tau)}} = 0. \tag{A.15}$$

We are only interested in the exponential part of the integral that remains after the saddle point integration has been performed because this will give the dominant transverse contribution of the integral. If the pre-exponential factors are desired one needs to expand S to second order and perform the resulting integrals over t' and K_z.

We will begin by treating ionization; the expression for the current will be derived in an analogous manner and will follow readily from the our ionization derivation. For ionization we have $t = \tau$ and thus, with the condition $K_z + A(\tau) = 0$ in equation (A.14), the remaining exponential term becomes,

$$e^{iS(\mathbf{K},\tau,\tau+i\delta)} = e^{i\int_{\tau+i\delta}^{\tau}\Big(\overline{E}_g+\varepsilon_\parallel\big(A(t'')-A(\tau)\big)\Big)dt''}. \tag{A.16}$$

Performing the change of variables $t'' = \tau + i\eta$ converts the integral in the exponent above to,

$$\begin{aligned}
&\int_{\tau+i\delta}^{\tau}\Big(\overline{E}_g+\varepsilon_\parallel\big(A(t'')-A(\tau)\big)\Big)dt'' \\
&= -i\int_0^{\delta}\Big(\overline{E}_g+\varepsilon_\parallel\big(A(\tau+i\eta)\big)-A(\tau)\Big)d\eta \\
&\approx -i\Big(\overline{E}_g+\frac{\Delta}{2}\Big)\delta + i\frac{\Delta}{2}\int_0^{\delta}\cos\big(iaF(\tau)\eta\big)d\eta
\end{aligned} \tag{A.17}$$

where, in the above expression we have used,

$$A(\tau+i\eta) - A(\tau) = \frac{F_0}{\omega_0}\Big(\cos\big(\omega_0(\tau+i\eta)\big) - \cos\big(\omega_0\tau\big)\Big). \tag{A.18}$$

Again using the trigonometric identity for $\cos(x+y)$ we can write,

$$\begin{aligned}
\cos\big(\omega_0(\tau+i\eta)\big) &= \cos\big(\omega_0\tau\big)\cos\big(i\omega_0\eta\big) \\
&\quad - \sin\big(\omega_0\tau\big)\sin\big(i\omega_0\eta\big) \\
&\approx \cos\big(\omega_0\tau\big) - i\omega_0\eta\sin\big(\omega_0\tau\big)
\end{aligned} \tag{A.19}$$

where we have approximated the terms in the first line above to first order as $\cos(i\omega_0\eta) \approx 1$ and $\sin(i\omega_0\eta) \approx i\omega_0\eta$. Our integral can now be expressed as,

$$\begin{aligned}\int_{\tau+i\delta}^{\tau} \Big(\overline{E}_g + \varepsilon_{\parallel}\big(A(t'') - A(\tau)\big)\Big)dt'' & \\ &\approx -i\Big(\overline{E}_g + \tfrac{\Delta}{2}\Big)\delta i\tfrac{\Delta}{2}\int_0^{\delta}\Big(1 + \tfrac{1}{2}\big(a_z F(\tau)\big)^2\eta^2\Big)d\eta \\ &\approx -i\overline{E}_g\delta + im_z^{-1}F^2(\tau)\tfrac{\delta^3}{6} \\ &\approx i\frac{\sqrt{m_z}\Big(2\overline{E}_g\Big)^{3/2}}{3F(\tau)} \end{aligned} \tag{A.20}$$

where, in obtaining equation (A.20) we have used the relation from equation (A.15) with the negative sign for δ and $m_z^{-1} = \Delta a_z^2/2$. Finally, inserting equation (A.20) into the exponent and replacing $F(\tau)$ with F_0 we can express the exponential part of the ionization rate as,

$$\dot{n}_c \propto \int dk_x dk_y \exp\big(-2\sqrt{m_z}(2\overline{E}_g)^{3/2}/3F_0\big). \tag{A.21}$$

Taylor expanding $\overline{E}_g^{3/2}$ gives,

$$\overline{E}_g^{3/2} \approx E_g^{3/2} + \frac{3}{2}\sqrt{E_g}\left(\frac{k_x^2}{2m_x} + \frac{k_y^2}{2m_y}\right). \tag{A.22}$$

After integration over $k_{x,y}$ we can split ionization into a rate $\dot{n}_c^{(3-q)D}(t)$ that is a combination of the longitudinal rate and the unconfined transverse term (should one exist) and a transverse contribution $n_\perp^{qD}$ from the confined direction(s) that is time-independent. The population is then given by,

$$\begin{aligned} n_c(t) &= \textstyle\int_{-\infty}^{t} \dot{n}_c^{(3-q)D}(t) n_\perp^{qD} dt' \\ &= n_\perp^{qD}\textstyle\int_{-\infty}^{t} \dot{n}_c^{(3-q)D}(t) dt' \\ &= n_\perp^{qD} n_c^{(3-q)D}(t) \end{aligned} \tag{A.23}$$

where $n_\perp^{qD}$ is given by,

$$n_\perp^{qD} = \left(\frac{F_0^2}{2m_z E_g}\right)^{q/4}\prod_{j=1}^{q} a_j\sqrt{\frac{m_j}{2\pi}}. \tag{A.24}$$

As with the text above, q denotes the number of confined transverse directions.

Turning our attention to the current, we can now write the integral in the exponent as the sum of two integrals. The first runs from $\tau + i\delta$ to τ and the second runs from τ to t; this is given as,

$$\begin{aligned}
&\int_{\tau+i\delta}^{t} \Big(\overline{E}_g + \varepsilon_{\parallel}\big(A(t'') - A(\tau)\big)\Big)dt'' \\
&= \int_{\tau+i\delta}^{\tau} \Big(\overline{E}_g + \varepsilon_{\parallel}\big(A(t'') - A(\tau)\big)\Big)dt'' \\
&\quad + \int_{\tau}^{t} \Big(\overline{E}_g + \varepsilon_{\parallel}\big(A(t'') - A(\tau)\big)\Big)dt''. \qquad \text{(A.25)}
\end{aligned}$$

The first integral on the right hand side is the same as that for equation (A.20). The second integral gives,

$$\begin{aligned}
&\int_{\tau}^{t} \Big(\overline{E}_g + \varepsilon_{\parallel}\big(A(t'') - A(\tau)\big)\Big)dt'' \\
&= \overline{E}_g(t-\tau) + \int_{\tau}^{t} \varepsilon_{\parallel}\big(A(t'') - A(\tau)\big)dt''. \qquad \text{(A.26)}
\end{aligned}$$

By writing the transverse band gap in the effective mass approximation we get,

$$\overline{E}_g \approx E_g + \frac{k_x^2}{2m_x} + \frac{k_y^2}{2m_y}. \qquad \text{(A.27)}$$

Further, $\overline{E}_g^{3/2}$ can be expanded as in equation (A.22) above. This allows us to express the 3D current j_{3D} as,

$$\begin{aligned}
j_{3D} \quad &\propto \textstyle\sum_\tau e^{-\frac{\sqrt{m_z}}{3F(\tau)}(2E_g)^{3/2}} e^{i\left(E_g(t-\tau)+\int_\tau^t \varepsilon_{\parallel}\left(A(t'')-A(\tau)\right)dt''\right)} \\
&\quad \times \textstyle\prod_{j=x,y} \sqrt{\frac{a_j}{2\pi}} \int_{-\infty}^{\infty} dk_j e^{-\left(\sqrt{\frac{m_z E_g}{2F_0^2}}+\frac{i}{2}(t-\tau)\right)\frac{k_j^2}{m_j}} \qquad \text{(A.28)}
\end{aligned}$$

where the summation is over all birth times τ.

In a manner similar to that used to arrive at equation (3.7), the expression in equation (A.28) can be split into an unconfined term $j_{(3-q)D}$ and a confined transverse term $j_\perp^{qD}$ where,

$$|j_\perp^{qD}|^2 = \left(\frac{2m_z E_g}{F_0^2} + \frac{\pi^2}{\omega_0^2}\right)^{-q/2} \prod_{j=1}^{q} a_j m_j. \qquad \text{(A.29)}$$

In arriving at equation (3.8), we have approximated the excursion time between birth time τ and recollision time t by $|t-\tau| \approx \pi/\omega_0$. The exact excursion time

is determined by saddle point integration of the integral resulting from the Fourier transform of the current from time to frequency domain. For the scaling argument developed here, it is sufficient to use an excursion time is on the order of a half cycle.

Appendix B

Impurity versus intraband harmonics

The HHG spectrum in Fig. 4.4 of the main manuscript contains contributions from both the intraband and impurity terms. Figure B.1 compares the individual contributions of each of these terms. The individual harmonic spectra are calculated by taking the absolute value squared of the Fourier transform of Eqs. (4.30) and (4.31). The harmonics generated by the impurity term are represented by the blue line and those generated by the intraband current are represented by the green line. In the above band gap range — harmonics with $n \geq 5$ — the spectrum is dominated by the impurity term by approximately 3 to 6 orders of magnitude, depending on the harmonic. The only exception is harmonic 5 where the impurity and intraband terms are comparable. In the below band gap regions, the impurity harmonics are the dominant signal. The red, dashed line in the figure represent the dipole moment which scales similarly to the impurity harmonic signal.

We note here that the density of impurities will have an effect on the intensities of the impurity and intraband harmonics. In our one-dimensional calculations we have an impurity density of approximately 10^{-3} impurities per lattice cite. In three dimensions this density would be approximately 10^{-9} and will likely result in a decrease of impurity harmonics relative to the intraband spectrum. In our one dimensional calculations the impurity harmonics range from 3 to 6 orders-of-magnitude above the intraband harmonics. As a result, a relative impurity density of around 10^{-6} corresponding to an impurity density of approximately 10^{16}cm^{-3} should be sufficient to still observe stronger impurity harmonics.

Further, there is another parameter that determines the strength of impurity versus intraband HHG, which is the laser intensity. For the intraband harmonics to

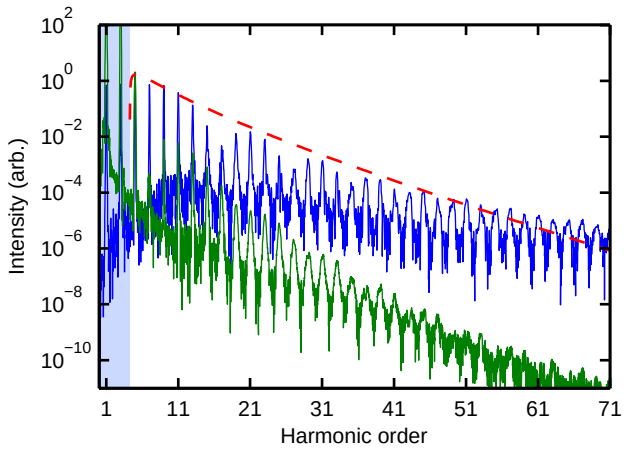

Figure B.1: The impurity (blue) and intraband (green) harmonic spectra. The red, dashed line represents the dipole moment. The shaded area indicates the below impurity ionization potential region. The dipole has been shifted on the y-axis to compare with the shape of the harmonic spectra.

develop, the electron must explore a significant portion of the nonlinear part of the band. Due to the low field intensities used here, the electron explores only about a third of the Brillouin zone and does not experience the full nonlinear portion of the conduction band, resulting in a reduction of the intensity of intraband harmonics. When the electron only explores a limited region of the Brillouin zone near the $\Gamma-$point, the intensity of the intraband harmonics decreases with harmonic order at a rate much larger than the impurity harmonics. The above discussion highlights the need for careful consideration when determining doping rates and laser parameters.

Appendix C

Numerical solution of the two-band equations

The integration of Eqs. (2.11) is numerically preformed using a fourth-order Runge-Kutta method [85]. The method is a numerical technique used to solve ordinary differential equation of the form

$$\dot{y} = f(y, t), \tag{C.1}$$

where the initial value of $y(0) = y_0$. At each time step, the solution is advanced as following,

$$y_{n+1} = y_n + \frac{h}{6}(k_1 + 2k_2 + 2k_3 + k_4) \tag{C.2}$$

$$t_{n+1} = t_n + h \tag{C.3}$$

where

$$\begin{aligned} k_1 =& f(t_n, y_n), \\ k_2 =& f(t_n + \frac{h}{2}, y_n + \frac{h}{2}k_1), \\ k_3 =& f(t_n + \frac{h}{2}, y_n + \frac{h}{2}k_2), \quad \text{and} \\ k_4 =& f(t_n + \frac{h}{2}, y_n + hk_3). \end{aligned} \tag{C.4}$$

To implement this method to Eqs. (2.11), we rewrite it in the form

$$\begin{aligned} \dot{b}_{c,\kappa} =& i\mathbf{F} \cdot \mathbf{d}^*(\mathbf{k}) b_{v,\kappa} \eta(\boldsymbol{\kappa}, t) \\ \dot{b}_{v,\kappa} =& i\mathbf{F} \cdot \mathbf{d}(\mathbf{k}) b_{c,\kappa} \eta^*(\boldsymbol{\kappa}, t) \\ \dot{\eta} =& i\varepsilon_g(\boldsymbol{\kappa}) \eta(\boldsymbol{\kappa}, t) \end{aligned} \tag{C.5}$$

where

$$\eta(\boldsymbol{\kappa}, t) = \exp[iS(\boldsymbol{\kappa}, t)]. \tag{C.6}$$

The system of equations C.5 is solved with the following initial conditions

$$\begin{aligned} b_v(\boldsymbol{\kappa}, 0) &= \frac{1}{\sqrt{2k_b}}, \\ b_c(\boldsymbol{\kappa}, 0) &= 0, \quad \text{and} \\ \eta(\boldsymbol{\kappa}, 0) &= 0. \end{aligned} \tag{C.7}$$

where $k_b = 2\pi/a$ is the reciprocal lattice vector and a is the lattice constant.

Appendix D

Atomic units and Conversion Factors

- Electron charge $(e) = 1.6021 \times 10^{-19}$ C
- Electron mass $(m) = 9.018 \times 10^{-31}$ kg
- Time $= a_0/v_0 = \hbar^3/me^4 = 2.4189 \times 10^{-17}$s
- Length : $a_0 = \hbar^2/me^2 = 5.2917 \times 10^{-11}$ m
- Energy $= e^2/a_0 = 4.3597 \times 10^{-18}$J $= 27.21$ eV
- Velocity : $v_0 = e^2/\hbar = 2.1877 \times 10^6$ m.s^{-1}
- Momentum: $= me^2/\hbar = 1.9926 \times 10^{-24}$ kg.m.s^{-1}
- Freqency $= v_0/a_0 = me^4/\hbar^3 = 4.1341 \times 10^{16}$ s^{-1}
- Electric potential $= e/a_0 = me^3/\hbar^2 = 27.21$ V
- Electric field strength : $F_0 = e/a_0^2 = m^2e^5/\hbar^4 = 5.142 \times 10^9$ V.cm^{-1}

Bibliography

[1] P. B. Corkum. Plasma perspective on strong field multiphoton ionization. *Phys. Rev. Lett.*, 71:1994–1997, Sep 1993.

[2] P áB Corkum and Ferenc Krausz. Attosecond science. *Nature physics*, 3(6):381, 2007.

[3] CD Lin, Anh-Thu Le, Zhangjin Chen, Toru Morishita, and Robert Lucchese. Strong-field rescattering physics—self-imaging of a molecule by its own electrons. *Journal of Physics B: Atomic, Molecular and Optical Physics*, 43(12):122001, 2010.

[4] David N Fittinghoff, Paul R Bolton, Britton Chang, and Kenneth C Kulander. Observation of nonsequential double ionization of helium with optical tunneling. *Physical review letters*, 69(18):2642, 1992.

[5] MB Gaarde, KJ Schafer, KC Kulander, B Sheehy, Dalwoo Kim, and LF DiMauro. Strong species dependence of high order photoelectron production in alkali metal atoms. *Physical review letters*, 84(13):2822, 2000.

[6] Barry Walker, Brian Sheehy, Kenneth C Kulander, and Louis F DiMauro. Elastic rescattering in the strong field tunneling limit. *Physical review letters*, 77(25):5031, 1996.

[7] Benjamin Wolter, Michael G Pullen, A-T Le, Matthias Baudisch, K Doblhoff-Dier, Arne Senftleben, Michael Hemmer, C Dieter Schröter, Joachim Ullrich, Thomas Pfeifer, et al. Ultrafast electron diffraction imaging of bond breaking in di-ionized acetylene. *Science*, 354(6310):308–312, 2016.

[8] Shambhu Ghimire, Anthony D DiChiara, Emily Sistrunk, Pierre Agostini, Louis F DiMauro, and David A Reis. Observation of high-order harmonic generation in a bulk crystal. *Nature physics*, 7(2):138, 2011.

[9] Tran Trung Luu, M Garg, S Yu Kruchinin, Antoine Moulet, M Th Hassan, and Eleftherios Goulielmakis. Extreme ultraviolet high-harmonic spectroscopy of solids. *Nature*, 521(7553):498, 2015.

[10] G Vampa, TJ Hammond, N Thiré, BE Schmidt, F Légaré, CR McDonald, T Brabec, and PB Corkum. Linking high harmonics from gases and solids. *Nature*, 522(7557):462, 2015.

[11] Georges Ndabashimiye, Shambhu Ghimire, Mengxi Wu, Dana A Browne, Kenneth J Schafer, Mette B Gaarde, and David A Reis. Solid-state harmonics beyond the atomic limit. *Nature*, 534(7608):520, 2016.

[12] Ben Zaks, Ren-Bao Liu, and Mark S Sherwin. Experimental observation of electron–hole recollisions. *Nature*, 483(7391):580, 2012.

[13] Olaf Schubert, Matthias Hohenleutner, Fabian Langer, Benedikt Urbanek, C Lange, U Huttner, D Golde, T Meier, M Kira, Stephan W Koch, et al. Sub-cycle control of terahertz high-harmonic generation by dynamical bloch oscillations. *Nature Photonics*, 8(2):119, 2014.

[14] Matthias Hohenleutner, Fabian Langer, Olaf Schubert, Matthias Knorr, U Huttner, SW Koch, M Kira, and Rupert Huber. Real-time observation of interfering crystal electrons in high-harmonic generation. *Nature*, 523(7562):572, 2015.

[15] D. Golde, T. Meier, and S. W. Koch. High harmonics generated in semiconductor nanostructures by the coupled dynamics of optical inter- and intraband excitations. *Phys. Rev. B*, 77:075330, Feb 2008.

[16] G. Vampa, C. R. McDonald, G. Orlando, D. D. Klug, P. B. Corkum, and T. Brabec. Theoretical analysis of high-harmonic generation in solids. *Phys. Rev. Lett.*, 113:073901, Aug 2014.

[17] G. Vampa, C. R. McDonald, G. Orlando, P. B. Corkum, and T. Brabec. Semiclassical analysis of high harmonic generation in bulk crystals. *Phys. Rev. B*, 91:064302, Feb 2015.

[18] Hanzhe Liu, Yilei Li, Yong Sing You, Shambhu Ghimire, Tony F Heinz, and David A Reis. High-harmonic generation from an atomically thin semiconductor. *Nature Physics*, 13(3):262, 2017.

[19] Murat Sivis, Marco Taucer, Giulio Vampa, Kyle Johnston, André Staudte, Andrei Yu Naumov, DM Villeneuve, Claus Ropers, and PB Corkum. Tailored semiconductors for high-harmonic optoelectronics. *Science*, 357(6348):303–306, 2017.

[20] Tengfei Huang, Xiaosong Zhu, Liang Li, Xi Liu, Pengfei Lan, and Peixiang Lu. High-order-harmonic generation of a doped semiconductor. *Physical Review A*, 96(4):043425, 2017.

[21] Dejan B. Milošević and Anthony F. Starace. Magnetic-field-induced intensity revivals in harmonic generation. *Phys. Rev. Lett.*, 82:2653–2656, Mar 1999.

[22] D Shafir, Y Mairesse, DM Villeneuve, PB Corkum, and N Dudovich. Atomic wavefunctions probed through strong-field light–matter interaction. *Nature Physics*, 5(6):412, 2009.

[23] Serguei Patchkovskii, Zengxiu Zhao, Thomas Brabec, and DM Villeneuve. High harmonic generation and molecular orbital tomography in multielectron systems: Beyond the single active electron approximation. *Physical review letters*, 97(12):123003, 2006.

[24] Caterina Vozzi, Matteo Negro, Francesca Calegari, Giuseppe Sansone, Mauro Nisoli, Sandro De Silvestri, and Salvatore Stagira. Generalized molecular orbital tomography. *Nature Physics*, 7(10):822, 2011.

[25] Jiro Itatani, Jérôme Levesque, Dirk Zeidler, Hiromichi Niikura, Henri Pépin, Jean-Claude Kieffer, Paul B Corkum, and David M Villeneuve. Tomographic imaging of molecular orbitals. *Nature*, 432(7019):867, 2004.

[26] Sarah Baker, Joseph S Robinson, CA Haworth, H Teng, RA Smith, CC Chirilă, Manfred Lein, JWG Tisch, and Jonathan P Marangos. Probing proton dynamics in molecules on an attosecond time scale. *Science*, 312(5772):424–427, 2006.

[27] Hans Jakob Wörner, Julien B Bertrand, Daniil V Kartashov, Paul B Corkum, and David M Villeneuve. Following a chemical reaction using high-harmonic interferometry. *Nature*, 466(7306):604, 2010.

[28] Hans Jakob Wörner, Julien B Bertrand, Baptiste Fabre, Julien Higuet, Hartmut Ruf, Antoine Dubrouil, Serguei Patchkovskii, Michael Spanner, Yann Mairesse, Valérie Blanchet, et al. Conical intersection dynamics in no2 probed by homodyne high-harmonic spectroscopy. *Science*, 334(6053):208–212, 2011.

[29] A. McPherson, G. Gibson, H. Jara, U. Johann, T. S. Luk, I. A. McIntyre, K. Boyer, and C. K. Rhodes. Studies of multiphoton production of vacuum-ultraviolet radiation in the rare gases. *J. Opt. Soc. Am. B*, 4(4):595–601, Apr 1987.

[30] M. Lewenstein, Ph. Balcou, M. Yu. Ivanov, Anne L'Huillier, and P. B. Corkum. Theory of high-harmonic generation by low-frequency laser fields. *Phys. Rev. A*, 49:2117–2132, Mar 1994.

[31] P. A. Franken, A. E. Hill, C. W. Peters, and G. Weinreich. Generation of optical harmonics. *Phys. Rev. Lett.*, 7:118–119, Aug 1961.

[32] Thomas Brabec and Ferenc Krausz. Intense few-cycle laser fields: Frontiers of nonlinear optics. *Rev. Mod. Phys.*, 72:545–591, Apr 2000.

[33] Robert W Boyd. *Nonlinear optics*. Elsevier, 2003.

[34] Peter Hawkins. High harmonic generation in periodic systems. 2016.

[35] Ryuji Morita and Mikio Yamashita. Relationship between second-and third-order nonlinear optical susceptibilities due to electronic polarization. *Japanese journal of applied physics*, 32(7A):L905, 1993.

[36] N. H. Burnett, H. A. Baldis, M. C. Richardson, and G. D. Enright. Harmonic generation in co2 laser target interaction. *Applied Physics Letters*, 31(3):172–174, 1977.

[37] LV Keldysh et al. Ionization in the field of a strong electromagnetic wave. *Sov. Phys. JETP*, 20(5):1307–1314, 1965.

[38] MV Ammosov. Mv ammosov, nb delone, and vp krainov, sov. phys. jetp 64, 1191 (1986). *Sov. Phys. JETP*, 64:1191, 1986.

[39] Jeffrey L. Krause, Kenneth J. Schafer, and Kenneth C. Kulander. High-order harmonic generation from atoms and ions in the high intensity regime. *Phys. Rev. Lett.*, 68:3535–3538, Jun 1992.

[40] K. J. Schafer, Baorui Yang, L. F. DiMauro, and K. C. Kulander. Above threshold ionization beyond the high harmonic cutoff. *Phys. Rev. Lett.*, 70:1599–1602, Mar 1993.

[41] T Pfeifer, Ch Spielmann, and G Gerber. Femtosecond x-ray science. *Reports on Progress in Physics*, 69(2):443, 2006.

[42] Charles G. Durfee, Andy R. Rundquist, Sterling Backus, Catherine Herne, Margaret M. Murnane, and Henry C. Kapteyn. Phase matching of high-order harmonics in hollow waveguides. *Phys. Rev. Lett.*, 83:2187–2190, Sep 1999.

[43] Misha Yu Ivanov, Thomas Brabec, and Neal Burnett. Coulomb corrections and polarization effects in high-intensity high-harmonic emission. *Physical Review A*, 54(1):742, 1996.

[44] See Leang Chin, Pierre Agostini, and Gaetano Ferrante. *Progress in Ultrafast Intense Laser Science III*, volume 89. Springer Science & Business Media, 2008.

[45] NW Ashcroft and ND Mermin. Solid state physics; thomson learning, inc. *Stamford, CT*, 1976.

[46] F Brunel. Harmonic generation due to plasma effects in a gas undergoing multiphoton ionization in the high-intensity limit. *JOSA B*, 7(4):521–526, 1990.

[47] Hartmut Haug and Stephan W Koch. *Quantum Theory of the Optical and Electronic Properties of Semiconductors*. WORLD SCIENTIFIC, 5th edition, 2009.

[48] C. R. McDonald, G. Vampa, P. B. Corkum, and T. Brabec. Interband bloch oscillation mechanism for high-harmonic generation in semiconductor crystals. *Phys. Rev. A*, 92:033845, Sep 2015.

[49] Paul Harrison and Alex Valavanis. *Quantum wells, wires and dots: theoretical and computational physics of semiconductor nanostructures*. John Wiley & Sons, 2016.

[50] Peter G. Hawkins, Misha Yu. Ivanov, and Vladislav S. Yakovlev. Effect of multiple conduction bands on high-harmonic emission from dielectrics. *Phys. Rev. A*, 91:013405, Jan 2015.

[51] Mengxi Wu, Shambhu Ghimire, David A. Reis, Kenneth J. Schafer, and Mette B. Gaarde. High-harmonic generation from bloch electrons in solids. *Phys. Rev. A*, 91:043839, Apr 2015.

[52] I Vurgaftman, J áR Meyer, and L áR Ram-Mohan. Band parameters for iii–v compound semiconductors and their alloys. *Journal of applied physics*, 89(11):5815–5875, 2001.

[53] Ü Özgür, Ya I Alivov, Chunli Liu, A Teke, MA Reshchikov, S Doğan, VCSJ Avrutin, S-J Cho, and H Morkoç. A comprehensive review of zno materials and devices. *Journal of applied physics*, 98(4):11, 2005.

[54] A Schleife, F Fuchs, C Rödl, J Furthmüller, and F Bechstedt. Band-structure and optical-transition parameters of wurtzite mgo, zno, and cdo from quasi-particle calculations. *physica status solidi (b)*, 246(9):2150–2153, 2009.

[55] Qimin Yan, Patrick Rinke, Momme Winkelnkemper, Abdallah Qteish, Dieter Bimberg, Matthias Scheffler, and Chris G Van de Walle. Strain effects and band parameters in mgo, zno, and cdo. *Applied Physics Letters*, 101(15):152105, 2012.

[56] CR McDonald, G Vampa, PB Corkum, and T Brabec. Intense-laser solid state physics: unraveling the difference between semiconductors and dielectrics. *Physical review letters*, 118(17):173601, 2017.

[57] Martin Schultze, Krupa Ramasesha, CD Pemmaraju, SA Sato, D Whitmore, A Gandman, James S Prell, LJ Borja, D Prendergast, K Yabana, et al. Attosecond band-gap dynamics in silicon. *Science*, 346(6215):1348–1352, 2014.

[58] Martin Schultze, Elisabeth M Bothschafter, Annkatrin Sommer, Simon Holzner, Wolfgang Schweinberger, Markus Fiess, Michael Hofstetter, Reinhard Kienberger, Vadym Apalkov, Vladislav S Yakovlev, et al. Controlling dielectrics with the electric field of light. *Nature*, 493(7430):75, 2013.

[59] Agustin Schiffrin, Tim Paasch-Colberg, Nicholas Karpowicz, Vadym Apalkov, Daniel Gerster, Sascha Mühlbrandt, Michael Korbman, Joachim Reichert, Martin Schultze, Simon Holzner, et al. Optical-field-induced current in dielectrics. *Nature*, 493(7430):70, 2013.

[60] Annkatrin Sommer, EM Bothschafter, SA Sato, Clemens Jakubeit, Tobias Latka, Olga Razskazovskaya, Hanieh Fattahi, Michael Jobst, W Schweinberger, Vage Shirvanyan, et al. Attosecond nonlinear polarization and light–matter energy transfer in solids. *Nature*, 534(7605):86, 2016.

[61] Takuya Higuchi, Christian Heide, Konrad Ullmann, Heiko B Weber, and Peter Hommelhoff. Light-field-driven currents in graphene. *Nature*, 550(7675):224, 2017.

[62] Yong Sing You, David A Reis, and Shambhu Ghimire. Anisotropic high-harmonic generation in bulk crystals. *Nature Physics*, 13(4):345, 2017.

[63] II EN Adams. Motion of an electron in a perturbed periodic potential. *Physical Review*, 85(1):41, 1952.

[64] Joaquin M Luttinger and Walter Kohn. Motion of electrons and holes in perturbed periodic fields. *Physical Review*, 97(4):869, 1955.

[65] W Kohn and JM Luttinger. Hyperfine splitting of donor states in silicon. *Physical Review*, 97(4):883, 1955.

[66] Sokrates T Pantelides. The electronic structure of impurities and other point defects in semiconductors. *Reviews of Modern Physics*, 50(4):797, 1978.

[67] Xiao-Min Tong, ZX Zhao, and Chii-Dong Lin. Theory of molecular tunneling ionization. *Physical Review A*, 66(3):033402, 2002.

[68] Tengfei Luo, Jivtesh Garg, Junichiro Shiomi, Keivan Esfarjani, and Gang Chen. Gallium arsenide thermal conductivity and optical phonon relaxation times from first-principles calculations. *EPL (Europhysics Letters)*, 101(1):16001, 2013.

[69] Yasushi Shinohara, Kazuhiro Yabana, Yosuke Kawashita, J-I Iwata, Tomohito Otobe, and George F Bertsch. Coherent phonon generation in time-dependent density functional theory. *Physical Review B*, 82(15):155110, 2010.

[70] Muneaki Hase, Masayuki Katsuragawa, Anca Monia Constantinescu, and Hrvoje Petek. Frequency comb generation at terahertz frequencies by coherent phonon excitation in silicon. *Nature photonics*, 6(4):243, 2012.

[71] BK Meyer, J Sann, DM Hofmann, C Neumann, and A Zeuner. Shallow donors and acceptors in zno. *Semiconductor Science and Technology*, 20(4):S62, 2005.

[72] Matthias C Hoffmann and József András Fülöp. Intense ultrashort terahertz pulses: generation and applications. *Journal of Physics D: Applied Physics*, 44(8):083001, 2011.

[73] Ml J Caldas, A Fazzio, and Alex Zunger. A universal trend in the binding energies of deep impurities in semiconductors. *Applied Physics Letters*, 45(6):671–673, 1984.

[74] W Boutu, Stefan Haessler, H Merdji, P Breger, G Waters, M Stankiewicz, LJ Frasinski, R Taieb, J Caillat, A Maquet, et al. Coherent control of attosecond emission from aligned molecules. *Nature Physics*, 4(7):545, 2008.

[75] VE Gruzdev. Photoionization rate in wide band-gap crystals. *Physical Review B*, 75(20):205106, 2007.

[76] PA Zhokhov and AM Zheltikov. Field-cycle-resolved photoionization in solids. *Physical review letters*, 113(13):133903, 2014.

[77] PA Zhokhov and AM Zheltikov. Depth-resolved subcycle dynamics of photoionization in solids. *Physical Review A*, 96(3):033415, 2017.

[78] Vitaly Gruzdev and Olga Sergaeva. Ultrafast modification of band structure of wide-band-gap solids by ultrashort pulses of laser-driven electron oscillations. *Physical Review B*, 98(11):115202, 2018.

[79] G Vampa. G. vampa, tj hammond, n. thiré, be schmidt, f. légaré, cr mcdonald, t. brabec, dd klug, and pb corkum, phys. rev. lett. 115, 193603 (2015). *Phys. Rev. Lett.*, 115:193603, 2015.

[80] Shicheng Jiang, Jigen Chen, Hui Wei, Chao Yu, Ruifeng Lu, and CD Lin. Role of the transition dipole amplitude and phase on the generation of odd and even high-order harmonics in crystals. *Physical Review Letters*, 120(25):253201, 2018.

[81] Keliang He, Nardeep Kumar, Liang Zhao, Zefang Wang, Kin Fai Mak, Hui Zhao, and Jie Shan. Tightly bound excitons in monolayer wse 2. *Physical review letters*, 113(2):026803, 2014.

[82] Alexey Chernikov, Timothy C Berkelbach, Heather M Hill, Albert Rigosi, Yilei Li, Ozgur Burak Aslan, David R Reichman, Mark S Hybertsen, and Tony F Heinz. Exciton binding energy and nonhydrogenic rydberg series in monolayer ws 2. *Physical review letters*, 113(7):076802, 2014.

[83] Isabella Floss, Christoph Lemell, Georg Wachter, Valerie Smejkal, Shunsuke A. Sato, Xiao-Min Tong, Kazuhiro Yabana, and Joachim Burgdörfer. Ab initio multiscale simulation of high-order harmonic generation in solids. *Phys. Rev. A*, 97:011401, Jan 2018.

[84] Paul M Koenraad and Michael E Flatté. Single dopants in semiconductors. *Nature materials*, 10(2):91, 2011.

[85] David Kincaid, David Ronald Kincaid, and Elliott Ward Cheney. *Numerical analysis: mathematics of scientific computing*, volume 2. American Mathematical Soc., 2009.